Title: Dual MAPK Inhibition Triggers Pro-inflammatory Signals and Sensitizes $BRAF^{V600E}$ Glioma to T Cell-Mediated Checkpoint Therapy

Authors: Yao Lulu Xing[1], Stefan Grossauer[3,4,†], Jong-Whi Park[1,2,†], Emon Nasajpour[1], Brandon Bui[1], Daniella Morales[1], Dena Panovska[1], Jeffrey J. Nirschl[5], Zhi-Ping Feng[6], Ruolun Wei[1,7], Katharina Koeck[3,4], Wes Thomason[8], Joanna Xiu[9], Patrick N. Harter[10], Katharina Filipski[11], Kelly Mahaney[1], Xuhuai Ji[12], Jean M. Mulcahy Levy[13], Gerald A. Grant[14], Laura M. Prolo[1], Kyle M. Walsh[15], Michael Lim[1], Dolores Hambardzumyan[8], Claudia K. Petritsch[1,‡,*]

Affiliations:

[1]Department of Neurosurgery, Stanford University, Palo Alto, CA 94305, USA.

[2]Department of Life Sciences, Gachon University, Incheon 21999, South Korea.

[3]Department of Neurosurgery, University of California San Francisco, San Francisco, CA94143, USA.

[4]Medical University of Vienna, Department of Neurosurgery, A-1090 Vienna, Austria.

[5]Department of Pathology, Stanford University, Palo Alto, CA 94305, USA.

[6]The Australian National University Bioinformatics Consultancy, John Curtin School of Medical Research, The Australian National University, ACT 2600, Australia.

[7]Department of Neurosurgery, Zhengzhou University First Affiliated Hospital, Henan 450000, China.

[8]Department of Oncological Sciences and Neurosurgery, Icahn School of Medicine at Mount Sinai, New York, NY 10029, USA.

[9]Medical Affairs, Caris Life Sciences Inc, Phoenix, Arizona, USA.

[10]Center for Neuropathology and Prion Research, University Hospital of Munich, LMU Munich, Munich, Germany.

[11]Neurological Institute (Edinger Institute), University Hospital, Frankfurt, Frankfurt am Main, Germany.

[12]Human Immune Monitoring Centre, Institute for Immunity, Transplantation, and Infection, Stanford University, Palo Alto, CA 94305, USA.

[13]Morgan Adams Foundation Brain Tumor Research Program, Departments of Hematology/Oncology, and Pediatrics, Children's Hospital of Colorado and University of Colorado, Aurora, Colorado, USA.

[14]Department of Neurosurgery, Duke University, Durham, North Carolina, USA

[15]Division of Neuro-Epidemiology, Department of Neurosurgery, Duke University, Durham, North Carolina, USA

[†]Equal Contribution

[‡]Lead Contact

*** Correspondence:** cpetri@stanford.edu (C.K.P.)

One Sentence Summary: Our findings show potential for combined BRAFi+MEKi treatment and dual immune checkpoint blockade to overcome resistance in BRAF mutant high-grade gliomas.

ABSTRACT: BRAF^{V600E} pediatric low-grade gliomas frequently transform into high-grade gliomas (HGG) and poorly respond to chemotherapy, resulting in high mortality. Although combined BRAF and MEK inhibition (BRAFi+MEKi) outperforms chemotherapy, ~70% of BRAF^{V600E} HGG patients are therapy resistant and undergo unbridled tumor progression. BRAF^{V600E} glioma have an immune-rich microenvironment suggesting that they could be responsive to immunotherapy but effects of BRAFi+MEKi on anti-tumor immunity are unclear. Using patient tumor tissue before and after BRAFi+MEKi, two novel syngeneic murine models of BRAF^{V600E} HGG, and patient-derived cell lines, we examined the effects of clinically relevant BRAFi+MEKi with dabrafenib and trametinib on tumor growth, cell states, and tumor-infiltrating T cells. We find that BRAFi+MEKi treatment : i) upregulated programmed cell death protein-1 (PD-1) signaling genes and PD-1 ligand (PD-L1) protein expression in murine BRAF^{V600E} HGG by stimulating IFNγ and IL-27, ii) attenuated T cell activity by IL-23, IL-27 and IL-32 production, which can promote the expansion of regulatory T cells, and iii) induced glial differentiation linked to a therapy-resistant PD-L1+ compartment through Galectin-3 secretion by tumor cells. Murine BRAF^{V600E} HGG shrinkage by BRAFi+MEKi is associated with the upregulation of interferon-gamma response genes, MHC class I/II expression, and antigen presentation and processing programs, indicative of increased anti-tumor immunity. Combined BRAFi+MEKi with therapeutic antibodies inhibiting the PD-1 and cytotoxic T-lymphocyte associated protein 4 (CTLA-4) immune checkpoints re-activate T cells and provide a survival benefit over single therapy in a T cell-dependent manner. The quadruple treatment overcame BRAFi+MEKi resistance by invigorating T cell-mediated anti-tumor immunity in murine BRAF^{V600E} HGG. PD-L1 expression was elevated in human BRAF-mutant versus BRAF-wildtype glioblastoma clinical specimen, complementing experimental findings and suggesting translational relevance for patient care.

INTRODUCTION:

High-grade gliomas (HGG) are the most prevalent malignant brain tumor in adults with a 50% mortality rate and the leading cause of cancer-related deaths in children [1-3]. Upregulation of mitogen-activated protein kinase (MAPK) pathway is a common glioma driver, an estimated 47.6% of gliomas across all ages and types and almost all pediatric gliomas [4] and prompting the development and clinical approval of multiple pharmacological inhibitors of MAPK pathway, most prominently of mutant BRAF kinase and MEK [5, 6]. $BRAF^{V600E}$ is a constitutively activated mutant BRAF kinase [7] found in pediatric low-grade gliomas (15-20%; LGGs) [8], pediatric high-grade gliomas (HGG) (~6%), and glioblastoma (GBM) (1-5%) in particular in epithelioid GBM (~50%) [9-13]. $BRAF^{V600E}$ is found in diverse histopathological entities, most commonly pleomorphic xanthoastrocytoma (PXA) and ganglioglioma (GG) [14] and is associated with poor response to chemotherapy [15-17] and high risk for transforming into HGG, especially with CDKN2A deletion [8, 18], resulting in a 10-year progression-free survival of <25% [8, 16].

In our preclinical data in a murine $BRAF^{V600E}$ glioma model (BRAF-2341) [19], combined BRAFi+MEKi is more effective at tumor shrinkage than BRAFi alone, facilitating FDA approval of $BRAF^{V600E}$ and MEK inhibitor combinations (BRAFi+MEKi) with dabrafenib (TAFINLAR) and trametinib (MEKINIST) as first-line therapy for $BRAF^{V600E}$ LGG [20]. BRAFi+MEKi increases objective response rates (ORRs) in $BRAF^{V600E}$ LGG to over 50% from 30% with chemotherapy, but ORRs for HGG remain moderate at 38% for grade III tumors and declining with age, and ~70% of $BRAF^{V600E}$ HGG exhibit resistance [21-24],necessitating the development of novel therapies particularly for the HGG patient population.

Pediatric brain tumors are considered to be immune inactive due to their low mutational burden [25], but an increased number of activated cytotoxic CD8+ T cells and elevated MHC class I and

programmed cell death protein-1 ligand (PD-L1) expression have been reported for $BRAF^{V600E}$-mutant versus BRAF-wildtype glioma [10, 26], suggestive of their immune-rich microenvironment and intrinsic sensitivity to immunotherapy. Indeed, elevated CD3+CD8+ T cell frequency correlates with improved patient survival in GBM [27].

Programmed cell death protein-1 (PD-1) and cytotoxic T-lymphocyte antigen-4 (CTLA-4) immune checkpoints are hijacked by cancer cells to circumvent anti-tumor immune response [28], while providing therapeutic opportunities for immune checkpoint inhibitors (ICI) [29, 30]. Despite encouraging data in mouse models [31, 32], therapeutic antibodies inhibiting PD-1 (nivolumab) show no survival benefits, when combined with standard therapy in GBM [33, 34] or with therapeutic antibodies against CTLA-4 (ipilimumab) against pediatric high-grade brain tumors [35]. Encouragingly, ICI is effective for replication-repair-deficient high-grade gliomas (RRD-HGG) and combined α-PD-1 treatment and MEK inhibition with trametinib shows promising immune synergism in a small number of patients [36]. Moreover, α-PD-1 + α-CTLA-4 was effective as second-line treatment after BRAFi+MEKi in $BRAF^{V600E}$ metastatic melanoma [37] [38]. Considering these data and the reported immunomodulatory effects of BRAFi+MEKi in solid cancers [39-42], it is important to investigate the modulatory effects of BRAFi+MEKi in gliomas despite their known immunosuppressive tumor microenvironment.

In this study, we investigated BRAFi+MEKi-regulated tumor cell and immune responses in two distinct types of syngeneic murine $BRAF^{V600E}$ HGG model (adenovirus-induced BRAF-2341/M34 and RCAS-induced RCAS-BRAF) to avoid model-specific bias. These models reflect varied patient responses, unlike previous studies using a single and therapy-responsive mouse model [19]. Expression profiles of matched patient tumor tissue, before and after BRAFi+MEKi, were analyzed alongside novel BRAFi+MEKi-treated patient-derived neurospheres, which may

better represent tumors than other established cancer cell lines [43]. A cohort of BRAF-mutant and BRAF-wildtype glioblastomas was also examined for PD-L1 mRNA and protein expression, a known albeit disputed biomarker of ICI response.

Our results found that BRAFi+MEKi treatment elevated programmed cell death protein-1 (PD-1) signaling in $BRAF^{V600E}$ HGG and GBM by enhancing the secretion of IL-27 and IFNγ. This treatment also increased glial differentiation linked to a therapy-resistant PD-L1+ compartment mediated by Galectin-3. BRAFi+MEKi treatment to responsive tumors also upregulated interferon-gamma response genes, MHC class I/II expression, and antigen presentation and processing programs, indicative of increased anti-tumor immunity and potentially linking elevated cytotoxicity and antigen presentation to therapy response. In contrast, therapy-resistant tumors exhibited a loss of cytotoxicity and impaired antigen presentation to T cells, which is attributed to the downregulation of IFNγ, leading to reduced expression of antigen-presenting machinery and diminished immune recognition. This can be overcome by concurrent BRAFi+MEKi and ICI treatment. Clinical specimens further revealed elevated PD-L1 RNA and protein expression in BRAF-mutant compared to BRAF-wildtype glioblastoma. Collectively, our parallel investigations of patient tumor material and high-fidelity murine models provide deep insights into the modulatory effects of BRAFi+MEKi and may hold promise for a rational strategy for treating a subset of glioma with the $BRAF^{V600E}$ mutation.

RESULTS:

Glial Differentiation Signatures Are Increased After BRAFi+MEKi Treatment

To investigate BRAFi+MEKi treatment effects, we analyzed $BRAF^{V600E}$ GBM from two patients before and after dabrafenib (BRAFi) and trametinib (MEKi) treatment using magnetic

resonance imaging (MRI), bulk RNA sequencing (RNA-seq) and immunofluorescence (IF) staining **(Fig. 1A, figs. S1A-C and table S1)**. MRI of patient 49 revealed a large tumor mass at diagnosis, a resection cavity with no visible tumor, and recurrence after chemoradiotherapy and BRAFi+MEKi treatment within only four months **(Fig. 1B, S1A)**. MRI of patient 12 revealed the first recurrence after chemoradiotherapy and the second recurrence after BRAFi+MEKi treatment adjacent to the resection cavity **(figs. S1B-C)**. Gene ontology analysis of bulk RNA-seq data from matched GBM tissue before and after BRAFi+MEKi showed upregulation of genes engaged in gliogenesis as well as synapse organization, axon development, extracellular matrix organization, and cell-substrate adhesion after BRAFi+MEKi treatment. Pathways associated with gliogenesis were significantly enriched for upregulated genes, including markers for pre-oligodendrocyte progenitor cells (pre-OPCs) (*ASCL1*, *HES6*, *EGFR*, *DLL1*), neural progenitors and neural stem cells (*PROM1/CD133*), astrocytes (*GFAP*, *AQP4)*, and oligodendrocytes (*PROM1/CD133*, *CLDN11*, *ASPA*, *CNP*, *MBP*, *PLP1*) **(Fig. 1C, fig. S1D)**. The increase in PROM1/CD133+ expression is consistent with our previous study identifying a CD133+ BRAF-inhibitor resistant cell population in $BRAF^{V600E}$ GBM [44]. Upregulation of selected glial cell markers was validated at the protein level by IF, showing increased expression of astrocyte marker GFAP, and oligodendrocyte markers MBP and OLIG2 but not PDGFRα in $BRAF^{V600E}$ GBM after treatment **(Figs. 1D-F)**.

Overall, our data showed that extensive treatment including BRAFi+MEKi enriched for pre-OPC and differentiated glia cell expression profiles and increased the abundance of PROM1/CD133+ cells.

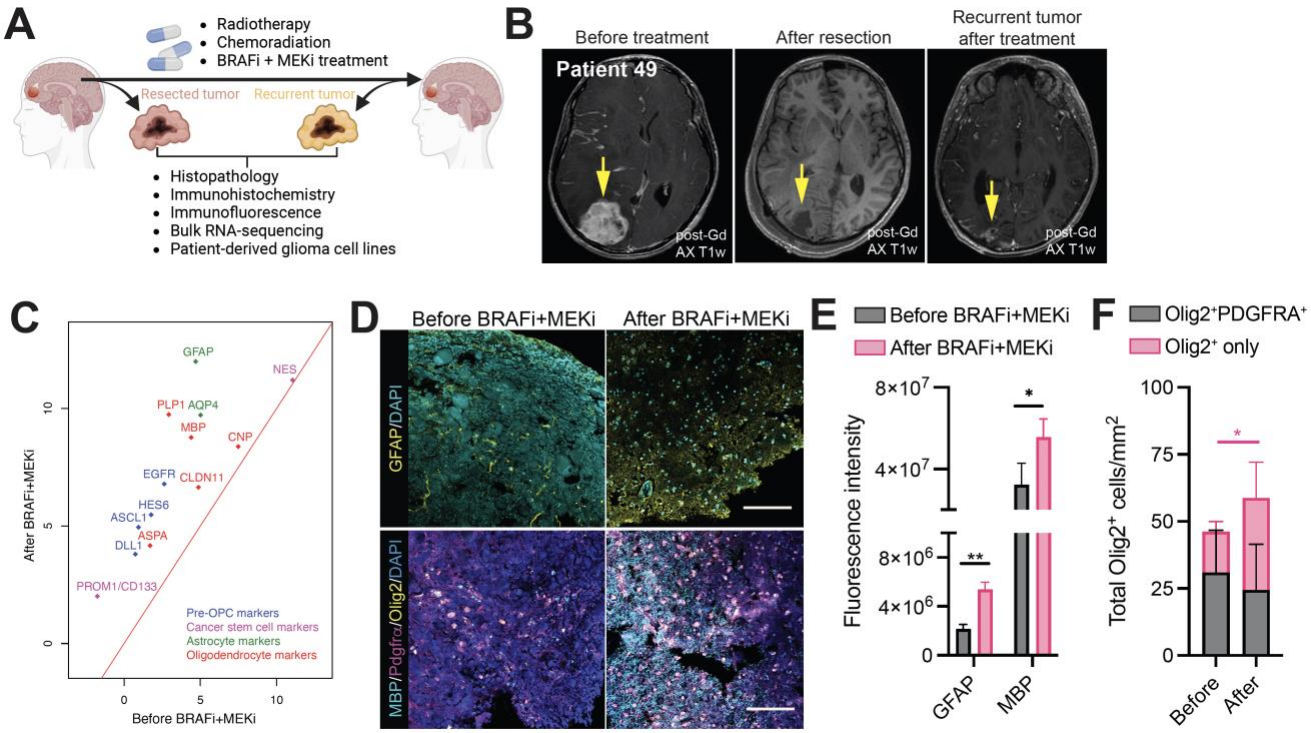

Figure 1: Glial Differentiation Signatures Are Increased After BRAFi+MEKi Treatment

(A) Schematic of longitudinal analyses of $BRAF^{V600E}$ GBM from two patients (49, 12).

(B) Contrast-enhanced (post-gadolinium) axial T1 MRI showing a large tumor mass (arrow, left panel) before treatment, a resection cavity without visible tumor after surgery (arrow, middle panel), and a recurrence predominantly in the leptomeningeal region (arrow, right panel) after treatment with chemoradiation and dabrafenib+trametinib (BRAFi+MEKi) in patient 49.

(C) The scatter plot of selected glial- and progenitor-related transcripts that are differentially expressed before and after treatment including BRAFi+MEKi from bulk RNA sequencing.

(D) Representative IF for astrocyte marker GFAP (top panels), and oligodendrocyte progenitor cell (OPC) marker PDGFRα and oligodendrocyte markers MBP and OLIG2 of $BRAF^{V600E}$ GBM before and after treatment with chemoradiation and dabrafenib+trametinib (BRAFi+MEKi). Scale bars: 180µm (top panel), 140µm (bottom panel).

(E) Quantification of GFAP and MBP intensities and

(F) PDGFRα+ and OLIG2+ cell frequencies in tumor field from (D).

*P<0.05 and **P<0.01 as assessed by unpaired two-tailed Student's t test.

Syngeneic Immunocompetent Mouse Models Recapitulate BRAF^{V600E} HGG Phenotypes

Next, we generated fully murine BRAF^{V600E} HGG in syngeneic mice with an intact immune system to systematically investigate BRAFi+MEKi effects. We bred cre-activatable knock-in allele (BRaf^{CA}) and the knock-out allele for murine Cdkn2a homologous locus Ink4a/Arf (Ink4a/Arf$^{flox/flox}$) [45] into C57BL/6 mice, because this genetic background is universally used for immunological studies **(Figs. 2A, 2G, table S2)**. As with our BRAF-2341 model which we previously generated in the FVB/N background [19], we injected adenovirus encoding cre recombinase (Ad-Cre) into the cortex of double-transgenic BRaf$^{CA/WT}$ Ink4a/Arf$^{flox/flox}$ adult mice, resulting in the simultaneous expression of BRAF^{V600E} and homozygous deletion of Ink4a/Arf (Ink4a/Arf$^{KO/KO}$) and development of BRaf^{V600E} Ink4a/Arf$^{KO/KO}$ gliomas after 54 days **(Fig. 2A, figs. S2A-B)**. To avoid model-specific bias, we generated a second model for BRAF^{V600E} HGG (RCAS-BRAF) by injecting replication-competent avian-like sarcoma (RCAS) virus expressing *BRAF^{V600E}* and *Tp53* short-hairpin RNA (shRNA) into Ntv-a mice. This drives simultaneous BRAF^{V600E} expression and deletion of TP53 in Nestin-positive neural progenitor cells and leads to formation of gliomas around 70 days post-injection **(Fig. 2G)**.

We subsequently isolated cells from an endogenous BRaf^{V600E} Ink4a/Arf$^{KO/KO}$ HGG (M34) and RCAS-BRAF HGG, and re-injected cell dissociates orthotopically into syngeneic C57BL/6 mice to generate large orthotopic gliomas **(Fig. 2A; table S2),** as visualized by MRI **(Figs. 2B-C, 2H)**. Histopathologic assessment of orthotopic tumors revealed features of high-grade astrocytic gliomas, including high nuclear pleomorphism, necrosis, and microvascular proliferation, with subtle model-specific differences **(Fig. 2D; table S2, figs. S2C, S2I; STAR Methods)**. All three models displayed high intra-tumoral heterogeneity, expressing markers like glial fibrillary protein (GFAP), pan-oligodendrocyte marker OLIG2, neural stem and progenitor and cancer stem cell

markers NESTIN and PROM1/CD133, and oligodendrocyte progenitor cell (OPC) markers PDGFRα and NG2 **(Figs. 2E-F, 2J, figs. S2C-H, S2J, table S2)**. Glial and neuronal markers are no longer lineage-restricted as in the normal brain but frequently co-expressed, in the RCAS-BRAF model, which is typical for HGG cells **(Fig. 2J)**. GFAP-positive reactive astrocytes and PDGFRα/NG2-positive glioma-associated OPCs, identified by lack of GFP or CRE expression, were found in all three models **(figs. S2C-D, S2I**). Interestingly, PROM1/CD133 was co-expressed not only with NESTIN, potentially marking cancer stem cells, but also with OLIG2 in BRAF-2341 and RCAS-BRAF, likely marking oligodendrocyte-like tumor cells in agreement with previous reports [46, 47], and consistent with a lower proliferation rate compared to the overall OLIG2+ population, which encompasses proliferative oligodendrocyte progenitor cells **(Fig. 2E middle panel, figs. S2F, S2H, S2J)**. Notably, OLIG2 staining is mostly cytoplasmic in HGG cells and nuclear in the normal brain parenchyma, consistent with a role for cytoplasmic OLIG2 protein in astrocyte differentiation **(fig. S2J)** [48].

Our two novel murine models (BRAF-M34 and BRAF-RCAS) recapitulate $BRAF^{V600E}$ HGG albeit with model-specific differences. These models provide robust preclinical tools, facilitating cross-model comparison and immunological studies due to their identical genetic background (C57BL/6).

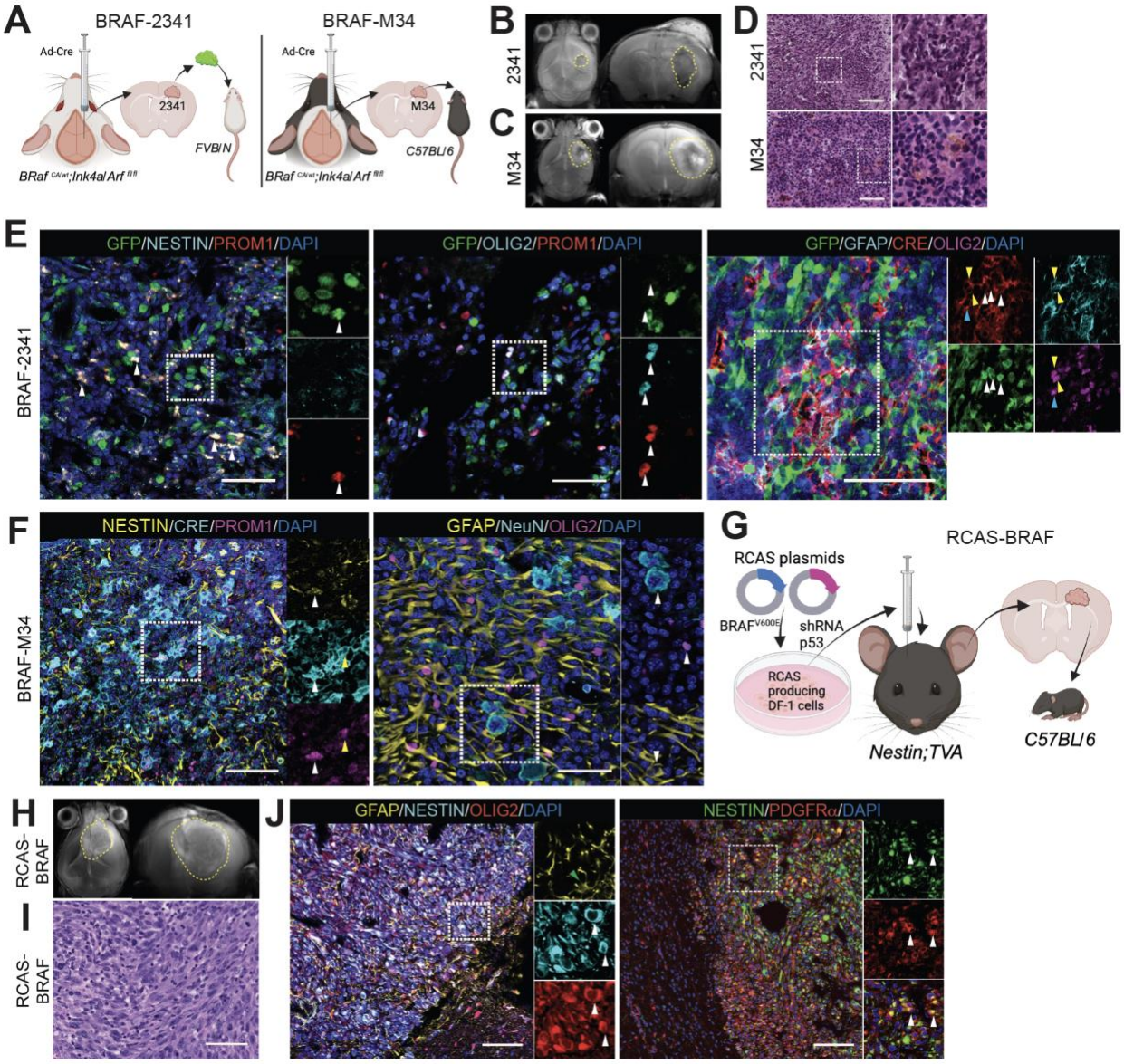

Figure 2: Novel Syngeneic Orthotopic Murine BRAF^{V600E} HGG Models

(A) Schematic diagram depicting the generation of murine BRAF^{V600E} CDKN2A-deleted HGG by adenovirus injection in immunocompetent mice with FVB/N (BRAF-2341) and C57BL/6 (BRAF-M34) genetic backgrounds. BRAF-2341 HGG cells were modified with lentivirus encoding GFP before orthotopic injection.

(B-C) Representative Z-projection of T2 weighted MRI scans in both axial and coronal orientations with yellow dashed lines outlining the tumor in the injected right hemisphere of mice with BRAF-2341 **(B)** and BRAF-M34 gliomas **(C)**.

(D) Low and high magnification images of H&E-stained coronal mouse brain sections of BRAF-2341 and BRAF-M34 HGG. Scale bars: 80µm (top panel), 60µm (bottom panel)

(E) Representative IF images of BRAF-2341. GFP and/or CRE expression identifies tumor cells (BRAF-2341). DNA is stained with DAPI in blue. Left panel: GFP and PROM1/CD133 double-positive cells representing HGG cells (white arrows). Middle panel: OLIG2 and PROM1/CD133 double-positive (GFP-negative) cells representing glioma-associated oligodendrocytes (white arrows). Right panel: Cre and GFP double-positive cells representing tumor cells (white arrows); tumor cells co-express GFAP and OLIG2 (yellow arrows); or OLIG2 alone (blue arrow). Single-channel images of the white-boxed area are shown next to the merged images. Scale bars: 60µm (left panel), 45µm (middle panel), 75µm (right panel).

(F) Representative IF images of BRAF-M34 HGG. Left panel: Cre, NESTIN, and PROM1/CD133 triple-positive cells representing neural progenitor/stem-like HGG cells or cancer stem cells (white arrows). Cre and PROM1/CD133 double-positive cells (negative for NESTIN) are potential oligodendrocyte-like tumor cells (yellow arrows). Right panel: NeuN, OLIG2, and GFAP single positive cells in the tumor core featured by hypercellularity (white arrows). Single-channel images of the white-boxed area are shown next to the merged images. Scale bars: 110µm (left panel), 50µm (right panel).

(G) Schematic diagram describing the generation of RCAS-induced $BRAF^{V600E}$ TP53-deleted (RCAS-BRAF) HGG in Nestin-Tva mice syngeneic with C57BL/6.

(H) Representative Z-projection of T2 weighted MRI scans in both axial and coronal orientations with yellow dashed outlines of the tumor infiltrating into the contralateral hemisphere.

(I) Representative H&E-stained coronal mouse brain section of orthotopic RCAS-BRAF HGG showing hypercellular proliferation of malignant ovoid to spindled cells arranged in fascicles and sheets. Scale bar: 140µm.

(J) Representative IF images of RCAS-BRAF. Tumors harbor GFAP positive astrocyte-like cells which are infrequently double-positive with OLIG2 (green arrow), and an abundance of NESTIN+ cells, which are frequently double-positive with OLIG2 (white arrows), and PDGFRα+ cells (white arrows). DAPI for DNA in blue. Single-channel images of the white-boxed area are shown next to the merged images. Scale bars: 90µm (left panel), 115µm (right panel).

BRAFi+MEKi Promotes Glial Differentiation of BRAF^{V600E} HGG cells.

BRAF^{V600E} HGG patients who recurred despite extensive treatment with chemoradiation and BRAFi+MEKi showed upregulation of genes linked to glial differentiation and a NESTIN+ and PROM1/CD133+ progenitor/stem cell compartment **(Fig. 1C, fig S1D)**. To investigate the effects of BRAFi+MEKi treatment *in vivo*, we treated syngeneic, orthotopic BRAF^{V600E} HGG-bearing mice (BRAF-2341) with BRAFi+MEKi (dabrafenib+trametinib) for up to 5 days followed by bulk RNA sequencing of HGG cells sorted for glial tumor marker A2B5 [47], flow cytometry and immunofluorescence (IF) for CD133/PROM1 and NESTIN **(Fig. 3A)**. BRAFi+MEKi treatment indeed increased transcripts for differentiated oligodendrocytes (*Mbp, Olig2, Cldn11, Btg2*) and astrocytes (*Gfap*) **(Fig. 3D)**, while neural and oligodendrocyte progenitor markers were downregulated *(Nes, Cspg4, Epn2, Pdgfrα*), and *Prom1/CD133* levels were unchanged **(data not shown)**. The frequency of NESTIN+ cells decreased after five days of BRAFi+MEKi treatment, consistent with transcriptome data, while the abundance of PROM1/CD133+ positive cells remained unchanged, as analyzed by flow cytometry and validated by IF **(Figs. 3A-C; fig. S3A)**. We concluded that NESTIN+ cells but not CD133/PROM1+ cells were eliminated by short-term treatment with BRAFi+MEKi, indicating that these two are distinct HGG cell populations. CD133/PROM1 cells appear to be less sensitive to BRAFi+MEKi treatment similar to the BRAFi-resistant PROM1/CD133+ cells we previously described [44]. Glial differentiation programs are upregulated with BRAFi+MEKi in these murine BRAF^{V600E} HGG consistent with results in human BRAF^{V600E} HGG **(Fig. 1)** and a patient-derived BRAF^{V600E} GBM cell line (SU-aGBM5) treated with BRAFi+MEKi treatment for 48 hours, although some species-specific differences in *MBP, OLIG2 and PDGFRα* expression were observed **(fig. S3B)**. We concluded that cancer stem cells

show initial, heterogenous sensitivity to BRAFi+MEKi and that glial differentiation is upregulated even with short-term treatment.

Next, we treated orthotopic BRAF^{V600E} HGG in our second mouse model (RCAS-BRAF) with BRAFi+MEKi (dabrafenib+trametinib) for 14 days followed by single-cell RNA sequencing and IF for validation. BRAFi+MEKi increased expression of glial differentiation markers (*Mbp, Clu, Btg2, Gfap*) and decreased expression of oligodendrocyte progenitor markers (*Cspg4, Pdgfrα*) **(Figs. 3E-G)**, consistent with the other murine BRAF^{V600E} HGG **(Fig. 3D)**. IF analyses confirmed upregulation of astrocyte marker GFAP and oligodendrocyte marker MBP, and downregulation of oligodendrocyte progenitor marker PDGFRα **(Figs. 3H-I),** further validating the durable increase in glial differentiation by BRAFi+MEKi treatment at the expense of oligodendrocyte progenitor cells in orthotopic BRAF^{V600E} HGG. Interestingly, although *Nes* mRNA was decreased, the frequency of NESTIN+ cells remained stable in BRAFi+MEKi-treated HGG tissue **(Fig. 3H)**, indicating that NESTIN+ cells may develop resistance to treatment over time, which is consistent with similar *NES* expression level after treatment in human HGG **(Fig. 1C)** and with NESTIN expression in therapy-resistant cancer stem cells [49].

To further validate the effects of BRAFi+MEKi treatment on glial differentiation we treated four BRAF^{V600E} HGG cell lines with dabrafenib and trametinib concurrently for 13 days (**figs. S4A-B)**. The two murine cell lines BRAF-M34 and RCAS-BRAF and two patient-derived cell lines STN-10049 (short STN-49) and SU-aGBM5 (aGBM5) were analyzed on day 13 of treatment by immunocytochemistry (ICC) with markers for myelinating oligodendrocyte MBP and pan-oligodendrocyte OLIG2 and NESTIN for neural progenitor/stem-like cells and cancer stem cells. As expected, BRAFi+MEKi treatment had visible negative effects on tumor cell viability of all four lines albeit to a different extent **(figs. S4C-F)**. BRAFi+MEKi treatment increased OLIG2+

and MBP+ cells abundance in murine and human patient-derived cell lines **(figs. S4C-F)**. The discrepancy between MBP expression in the human cell line SU-aGBM5 could be explained by species-specific differences in glial differentiation timing and propensity, since adding differentiation-inducing medium increased MBP expression levels after BRAFi+MEKi treatment. These data confirmed that BRAFi+MEKi increased abundance of differentiated glia cells (p-value < 0.05). Moreover, NESTIN+ cell frequency was high at baseline (vehicle-treatment) and remained stable after BRAFi+MEKi treatment in murine HGG cells and was significantly increased in human HGG cells **(figs. S4C-F)**.

Taken together, our data clearly show that BRAFi+MEKi treatment consistently increased the abundance of mature glial cells at the expense of oligodendrocyte progenitor cells, while cancer stem cells increased with longer treatment with NESTIN+ and CD133/PROM1+ marking two distinct cancer stem cell compartments associated with therapy escape.

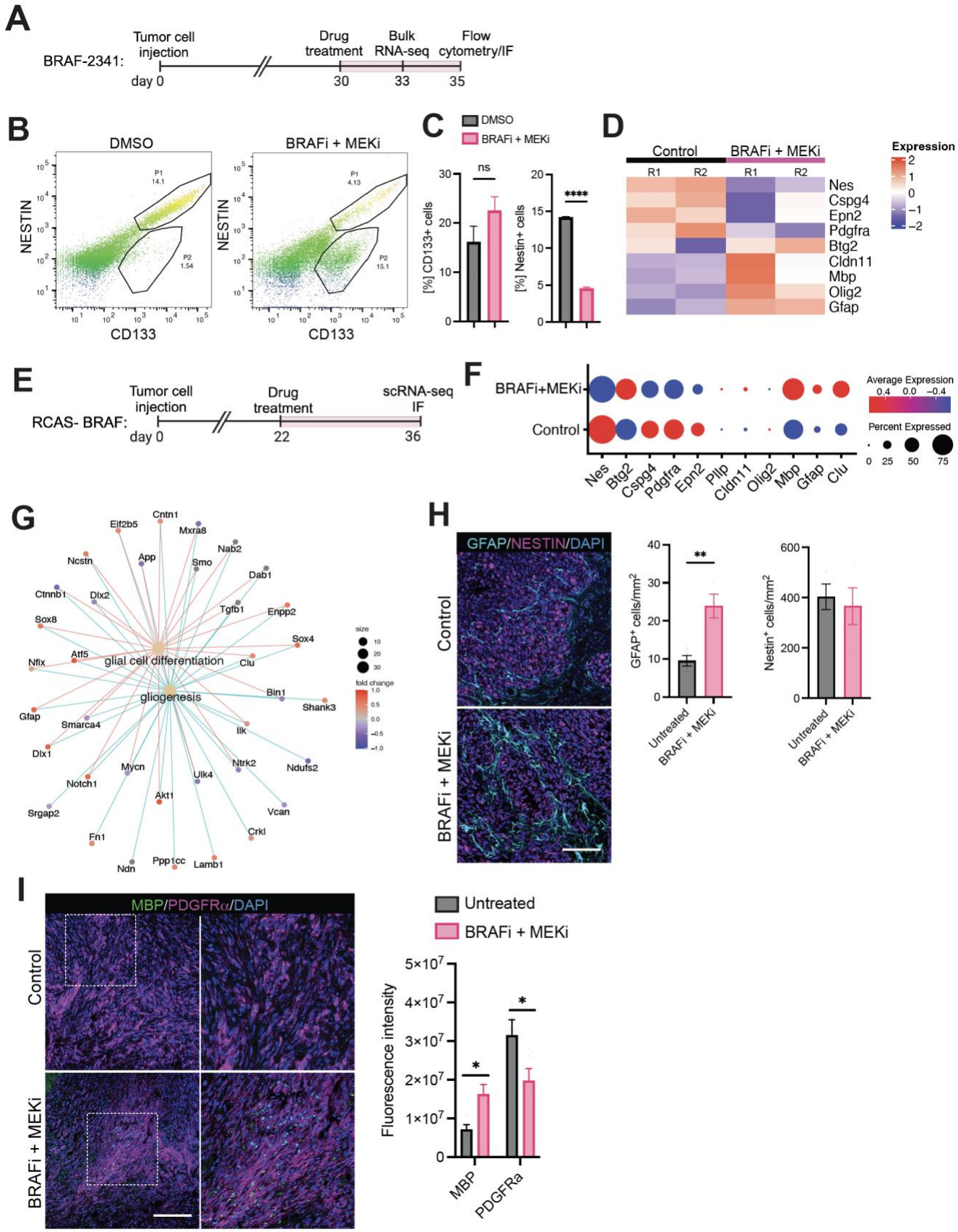
A
BRAF-2341:
Tumor cell injection
Drug treatment
Bulk RNA-seq
Flow cytometry/IF
day 0
30
33
35
B
DMSO
BRAFi + MEKi
NESTIN
CD133
P1 14.1
P2 1.54
P1 4.13
P2 15.1
C
DMSO
BRAFi + MEKi
ns
****
[%] CD133+ cells
[%] Nestin+ cells
D
Control
BRAFi + MEKi
R1
R2
Expression
Nes
Cspg4
Epn2
Pdgfra
Btg2
Cldn11
Mbp
Olig2
Gfap
E
RCAS- BRAF:
Tumor cell injection
Drug treatment
scRNA-seq IF
day 0
22
36
F
BRAFi+MEKi
Control
Average Expression
Percent Expressed
Nes
Btg2
Cspg4
Pdgfra
Epn2
Plip
Cldn11
Olig2
Mbp
Gfap
Clu
G
glial cell differentiation
gliogenesis
size
fold change
H
GFAP/NESTIN/DAPI
Control
BRAFi + MEKi
**
GFAP+ cells/mm2
Nestin+ cells/mm2
Untreated
BRAFi + MEKi
I
MBP/PDGFRα/DAPI
Control
BRAFi + MEKi
Untreated
BRAFi + MEKi
Fluorescence intensity
MBP
PDGFRa

316

Figure 3. BRAFi+MEKi increases differentiated glia cell abundance in BRAF^{V600E} HGG.

(A) Experimental timeline schematic for BRAFi+MEKi treatment in the murine BRAF-2341 model with analyses by bulk RNA sequencing of HGG cells, Flow Cytometry, and immunofluorescence (IF).

(B) Representative flow cytometry dot plots for HGG cells stained for PROM1/CD133 and NESTIN from mice treated as described in (A). Control-treated cells (DMSO) on the left. BRAFi+MEKi-treated cells on the right. P1 = PROM1/CD133 and NESTIN double-positive. P2 = PROM1/CD133-positive, NESTIN-negative.

(C) Quantification of flow cytometry analysis. ****P<0.0001 as assessed by unpaired t-test. ns, not significant.

(D) Expression levels of transcripts associated with glial cell differentiation were assessed in BRAF-2341 HGG cells treated with BRAFi+MEKi for three days. "R" denotes biological replicates.

(E) Experimental timeline schematic for a 14-day BRAFi+MEKi treatment in the RCAS-BRAF mouse model and analyses by single-cell RNA sequencing (scRNA-seq) of resected tumors and immunofluorescence (IF).

(F) Dot plot of scRNA-seq data showing upregulation of oligodendrocyte (*Mbp, Plp, Cldn11, Btg2*) and astrocyte (*Gfap, Clu*) differentiation transcripts, while oligodendrocyte progenitor (*Cspg4, Pdgfra, Epn2*) and cancer stem cell markers (*Nes*) are downregulated. The circle diameter indicates the percent marker expression in tumor cells.

(G) Cnetplot showing enrichment of transcripts related to glial cell differentiation and gliogenesis from gene ontology analysis of the scRNA-seq dataset from RCAS-BRAF HGG.

(H) Representative IF images of RCAS-BRAF HGG stained for GFAP, NESTIN, and DAPI (DNA) with control (vehicle) and BRAFi+MEKi treatment; quantitative data is shown on the right. Scale bar: 120µm.

(I) Representative IF images of RCAS-BRAF HGG stained for MBP, PDGFRα, and DAPI (DNA) with control (vehicle) and BRAFi+MEKi treatment. High magnification images of the white boxed areas; quantitative data is shown on the right. Scale bar: 170µm.

BRAFi+MEKi Treatment Induces Interferon Response Pathways in BRAF^{V600E} HGG.

Next, we investigated the effects of BRAFi+MEKi treatment on BRAF^{V600E} HGG further by conducting differential expression analyses and gene set enrichment analysis (GSEA) on our bulk RNA-seq data obtained from the patient-derived SU-aGBM5 cell line. This analysis revealed an upregulation of genes enriched in interferon-alpha (IFNα) and gamma (IFNγ) response signatures as well as extracellular matrix organization **(Figs. 4A-B, fig. S5A)**. IFNs have both pro-tumoral and anti-tumoral roles in the glioma microenvironment [50, 51]. IFNγ plays an important role in inducing tumor cell apoptosis, antigen presentation, and modulating the extracellular matrix [52]. Specifically, BRAFi+MEKi treatment upregulated major histocompatibility complex (MHC), along with other IFN response-related transcripts, such as those associated with inflammation. We observed upregulation of 67 IFN-γ response-associated transcripts common to both mouse (BRAF-2341) and human (SU-aGBM5) BRAF^{V600E} HGG after BRAFi+MEKi treatment **(Fig. 4B)**. The upregulation of selected MHC class I and class II genes, such as *HLA-A*, *HLA-B*, *HLA-DRA*, and *CIITA*, a known transcriptional regulator of MHC genes, was validated by qRT-PCR in two BRAF^{V600E} patient-derived HGG cell lines (SU-aGBM5, STN-49) **(figs. S5B-C),** as well as in murine BRAF-2341 cell line **(fig. S5D-F)**.

In conclusion, these *in vitro* data predict that BRAFi+MEKi will increase antigen presentation and T cell-mediated cytotoxicity and inflammation *in vivo*.

BRAFi+MEKi Boosts PD-1 Signaling, PD-L1 Expression and T Cell Infiltration in BRAF^{V600E} HGG

Next, we investigated the PD-1 immune checkpoint pathway in greater detail due to its clinical importance as an immunotherapy target. Reactome pathway analyses of bulk RNA-seq data from both human and murine BRAF^{V600E} HGG cell lines (SU-aGBM5 and BRAF-2341) identified PD-1 signaling as one of the most significantly altered pathways following BRAFi+MEKi treatment **(Fig. 4C, fig. S6A)**. Network analyses showed altered expression of multiple components of the PD-1 signaling pathway **(Fig. 4D, fig. S6B)** and immune regulatory pathways **(fig. S6C)**. PD-L1 expression was detected on murine and human patient-derived BRAF^{V600E} HGG cell lines and PD-L1 expression levels were significantly increased by BRAFi+MEKi treatment compared with vehicle (DMSO) treatment as control **(Fig. 4E)**. Moreover, PD-L1 protein was upregulated in human BRAF^{V600E}-mutant HGG tumor (patient 49) and *PD-L1 (Cd274)* transcript was elevated in BRAF^{V600E}-mutant HGG tumor (patient 12) after BRAFi+MEKi treatment **(Figs. 4F, 7E)**.

We then tested whether PD-L1 is co-expressed with NESTIN and differentiated oligodendrocytes, since we have found these cell types to be enriched by BRAFi+MEKi treatment. Indeed, 83% of NESTIN+ cells co-express PD-L1 in murine BRAF^{V600E} HGG **(fig. S7A)**. Interestingly, we observed that PD-L1 was highly co-expressed with oligodendrocyte markers MBP or OLIG2 in both the BRAF-M34 and RCAS-BRAF cell lines **(fig. S7B),** indicative of a link with glial differentiation and PD-L1 expression.

Expression of PD-L1 on tumor cells is known to be linked to the presence of T cells in the tumor microenvironment. To assess the T cell tumor infiltrate, we visualized T cells in murine BRAF^{V600E} HGG by IF and quantified their abundance in the tumor field. We simultaneously

determined the proportion of T cells positive for immune checkpoints PD-L1 and cytotoxic T-lymphocyte associated protein (CTLA-4), because their expression on T cells inhibits activated T cells. Effector T cells (T_{eff}, $CD4^+$, $CD8^+$) and regulatory T cells (Treg $CD4^+FoxP3^+$) were infiltrating the tumor mass **(Figs. 4G-H, figs. S6D, S7C)**, consistent with earlier studies that have identified a higher frequency of $CD3^+CD8^+$ T cells and a lower frequency of $CD3^+$ $FOXP3^+$ inhibitory, regulatory T cells (T_{regs}) in human BRAF-altered glioma, as compared to BRAF wildtype astrocytoma [26]. BRAFi+MEKi increased the frequency of CD4+ and CD8+ T cells, consistent with increased anti-tumor T cell-mediated cytotoxicity, and simultaneously elevated the fraction of PD-L1-positive T cells **(Figs. 4G-H)**, which suggests immune checkpoint-mediated inhibition of T cell activity after BRAFi+MEKi treatment.

These data indicate that $BRAF^{V600E}$ HGG exploits the PD-1 immune checkpoint to suppress anti-tumor immunity by inhibiting their T cell immune infiltrate with BRAFi+MEKi activating T cells while simultaneously limiting their activity through upregulation of PD-L1.

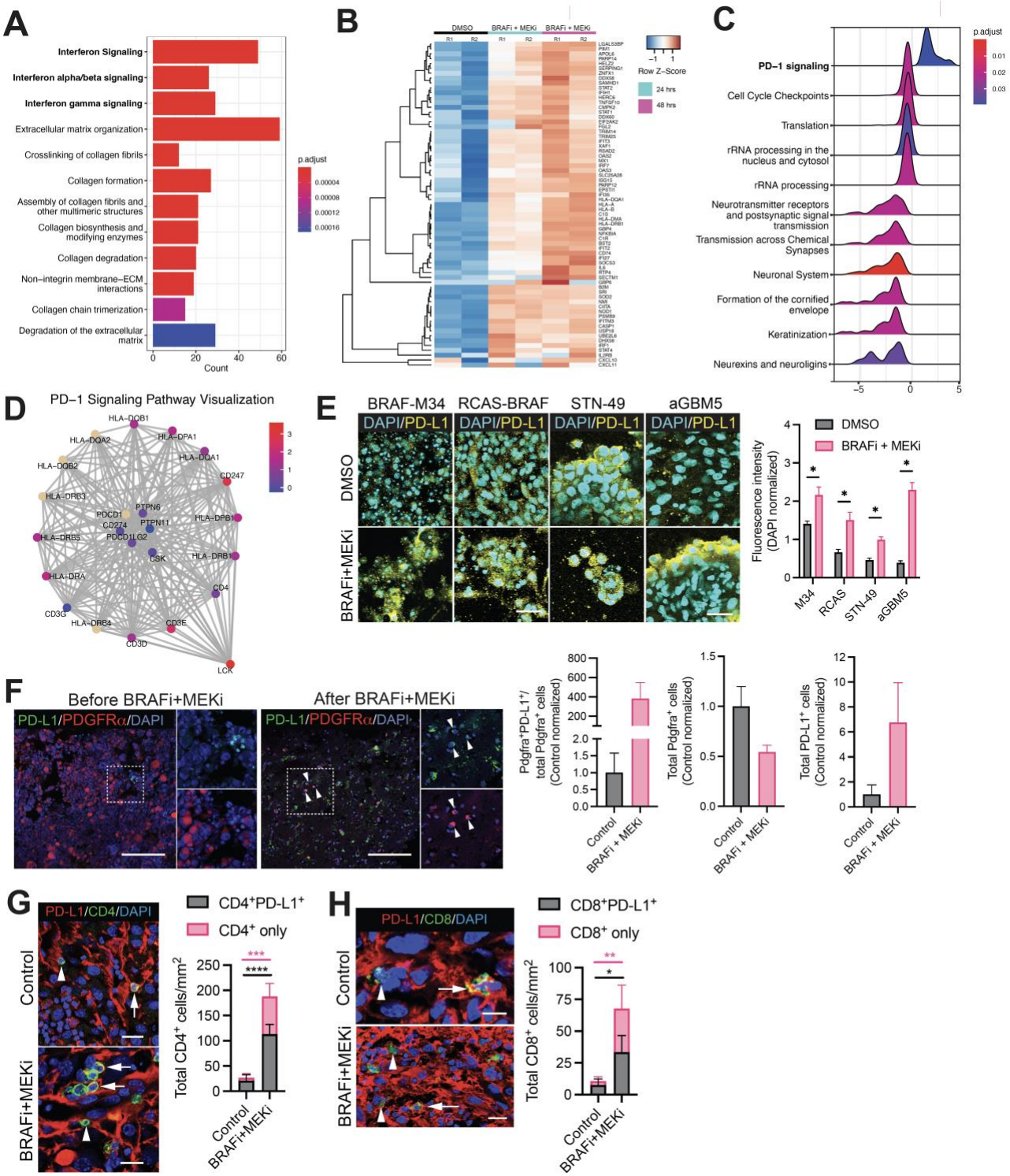
A
Interferon Signaling
Interferon alpha/beta signaling
Interferon gamma signaling
Extracellular matrix organization
Crosslinking of collagen fibrils
Collagen formation
Assembly of collagen fibrils and other multimeric structures
Collagen biosynthesis and modifying enzymes
Collagen degradation
Non–integrin membrane–ECM interactions
Collagen chain trimerization
Degradation of the extracellular matrix
Count
p.adjust
B
DMSO
BRAFi + MEKi
BRAFi + MEKi
Row Z–Score
24 hrs
48 hrs
C
PD–1 signaling
Cell Cycle Checkpoints
Translation
rRNA processing in the nucleus and cytosol
rRNA processing
Neurotransmitter receptors and postsynaptic signal transmission
Transmission across Chemical Synapses
Neuronal System
Formation of the cornified envelope
Keratinization
Neurexins and neuroligins
p.adjust
D
PD–1 Signaling Pathway Visualization
HLA–DQB1
HLA–DQA2
HLA–DPA1
HLA–DQA1
HLA–DQB2
CD247
HLA–DRB3
PTPN6
PDCD1
CD274
PTPN11
HLA–DPB1
HLA–DRB5
PDCD1LG2
CSK
HLA–DRB1
HLA–DRA
CD4
CD3G
HLA–DRB4
CD3E
CD3D
LCK
E
BRAF-M34
RCAS-BRAF
STN-49
aGBM5
DAPI/PD-L1
DMSO
BRAFi+MEKi
Fluorescence intensity (DAPI normalized)
DMSO
BRAFi + MEKi
M34
RCAS
STN-49
aGBM5
F
Before BRAFi+MEKi
After BRAFi+MEKi
PD-L1/PDGFRα/DAPI
Pdgfra+PD-L1+/ total Pdgfra+ cells (Control normalized)
Total Pdgfra+ cells (Control normalized)
Total PD-L1+ cells (Control normalized)
Control
BRAFi + MEKi
G
PD-L1/CD4/DAPI
Control
BRAFi+MEKi
CD4+PD-L1+
CD4+ only
Total CD4+ cells/mm2
Control
BRAFi+MEKi
H
PD-L1/CD8/DAPI
Control
BRAFi+MEKi
CD8+PD-L1+
CD8+ only
Total CD8+ cells/mm2
Control
BRAFi+MEKi

421

Figure 4. BRAFi + MEKi induces interferon response pathways and boosts PD-1 Signaling, PD-L1 Expression and T Cell Infiltration in BRAF^{V600E} HGG.

(A) Differential expression analysis and gene set enrichment analysis (GSEA) of gene expression data from the patient-derived SU-aGBM5 cell line revealed significant upregulation of genes associated with interferon signaling and extracellular matrix organization after 48 hours of BRAFi+MEKi treatment.

(B) Heatmap demonstrating significant increases in expression of IFN-γ response-associated transcripts after BRAFi+MEKi treatment compared with vehicle treatment at two different timepoints (24 hours and 48 hours). These 67 IFN-γ response-associated transcripts are also upregulated in BRAF-2341 with BRAFi+MEKi. R: technical replicate.

(C) Ridge plot of significantly upregulated Reactome pathways in human BRAF^{V600E} HGG cells (SU-aGBM5) after BRAFi+MEKi treatment for 48 hrs.

(D) Visualization of PD-1 signaling network changes in human BRAF^{V600E} HGG cells (SU-aGBM5) comparing BRAFi+MEKi treatment with vehicle (DMSO) treatment as control.

(E) Representative ICC images of murine and patient-derived tumor cells treated with BRAFi+MEKi and vehicle (DMSO) as controls, for 13 days, and subsequently stained for PD-L1. Quantification of (C). *P<0.05 as determined by multiple paired t-tests. Scale bar: 40µm.

(F) Representative IF images of human BRAF^{V600E} HGG (patient 49) tissue before and after treatment stained for PD-L1 and PDGFRα. DNA stained with DAPI in blue. Scale bars = 180µm (top panel), 180µm (bottom panel).

Quantification of (F).

(G-H) Representative IF images of RCAS-BRAF HGG stained for PD-L1, CD4 **(G)**, and CD8 **(H)**. Arrows indicate CD4^{+} and CD8^{+} cells positive for PD-L1 whereas triangles indicate CD4^{+}

and $CD8^+$ cells negative for PD-L1. Quantifications of cell populations after BRAFi+MEKi treatment compared with vehicle control treatment. *P < 0.05, **P<0.01, ***P<0.001, ****P<0.0001 as determined by two-way ANOVA with Sidak's multiple comparisons test. DNA is stained with DAPI in blue. Scale bars: (I) 20µm (left panel), 15µm (right panel), (J) 10µm (top panel), 20µm (bottom panel).

BRAFi+MEKi Cooperates with Immune Checkpoint Inhibition to Increase Survival and Overcome Therapy Resistance in a T cell-dependent Manner.

Our findings that $BRAF^{V600E}$ HGG expresses PD-L1 and CTLA-4 and that PD-1//PD-L1 expression is upregulated by BRAFi+MEKi treatment led us to assess the antitumor effects of combined BRAFi+MEKi and immune checkpoint inhibition (ICI) **(Fig. 5A)**. Syngeneic orthotopic $BRAF^{V600E}$ HGG-bearing mice were treated concurrently with dabrafenib and trametinib (BRAFi+MEKi), and/or with a combination of anti-PD-L1 (α-PD-L1) and anti-CTLA-4 (α-CTLA-4) therapeutic antibodies **(Fig. 5A)**. High-dimensional single-cell mass cytometry (CyTOF) analyses showed an increase in intra-tumoral $CD4^+$ and $CD8^+$ T_{eff} cells by BRAFi+MEKi treatment **(Figs. 5B-C)**, consistent with our findings in the RCAS-BRAF model **(Figs. 4G-H, figs. S8A-B)**. The frequency of CD4+ and CD8+ T cells expressing immune checkpoint molecules PD-1 and CTLA-4 was significantly increased with BRAFi+MEKi **(Figs. 5D-E)** and the increase could be reversed by concurrent BRAFi+MEKi and α-PD-L1 + α-CTLA-4 (quadruple treatment) which also reduced T_{reg} frequency (**Figs. 5D-E, figs. S8A-B**). We concluded that BRAFi+MEKi treatment activates T cells - consistent with an upregulated IFNα/γ signature in tumor cells **(Fig 4)** - and simultaneously induces T cell inhibition by upregulation of PD-1 and CTLA-4 immune checkpoints in T cells and glial differentiated and NESTIN+ tumor cells **(Fig. 4)**.

Quadruple treatment de-inhibited T cells **(Fig. 5E)** and provided significant survival benefit over BRAFi+MEKi or ICI alone in one $BRAF^{V600E}$ HGG model (BRAF-2341), extending survival to 150 days compared to 70 days with BRAFi+MEKi or ICI **(Fig. 5F, Table S3)**. Interestingly, the survival benefits of therapeutic antibodies alone and combinatorial effects with BRAFi+MEKi were completely abolished in athymic mice which lack thymus and T cells, suggesting T cell-mediated anti-tumor efficacy by therapeutic antibodies **(Fig. 5G).**

BRAFi+MEKi Synergizes with Immune Checkpoint Inhibition to Reactivate T cells and Overcome Therapy Resistance.

Interestingly, the survival benefit of quadruple treatment was validated in our independent $BRAF^{V600E}$ HGG model (RCAS-BRAF), which exhibits resistance to BRAFi+MEKi or ICI treatment. Nevertheless, quadruple treatment significantly prolonged the survival, indicating drug synergism **(Fig. 5H, Table S3)**. To understand the effects of quadruple treatment on T cells, we analyzed $CD4^+$ and $CD8^+$ T cell clusters by mining scRNA-seq data from the RCAS-BRAF model after treatment **(Figs. 5A, 5I-K)**. Several significant changes were observed, explaining why quadruple treatment, but not BRAFi+MEKi or ICI alone, provides a survival benefit. BRAFi+MEKi treatment moderately upregulated *Cd274* (*PD-L1)* and robustly upregulated *Cd276, Eomes, Socs, Fas* and *Fasl,* markers of T cell inhibition and apoptosis, in both $CD4^+$ and $CD8^+$ T cell clusters **(Fig. 5I)**. Additionally, *Foxp3* was upregulated in $CD4^+$ T cells after BRAFi+MEKi treatment, indicating the expansion of T_{reg} cells **(Fig. 5I)**. BRAFi+MEKi treatment downregulated *Gzmk*, *Gzmb*, *IL2ra*, and other activation markers in $CD4^+$ T cells, while upregulating *Cd27*, *Cd7,* and *Tnfrsf4* in $CD8^+$ T cells **(Fig. 5J)**, suggesting the presence of immunosuppressive $CD8^+$ T_{regs} or dysfunctional $CD8^+$ T cells [53]. MHC class I/II gene expression was dampened in $CD4^+$ and $CD8^+$ T cells, indicating that antigen presentation was not increased with BRAFi+MEKi treatment in the RCAS-BRAF model **(Fig. 5K)**.

ICI treatment led to upregulation of *Foxp3*, *Btla* (associated with T_{reg} expansion), and *Pdcd1*, *Lag3* (associated with dysfunctional $CD8^+$ T cells) **(Figs. 5I-J)**. $CD4^+$ T cells showed increased expression of *Ctla4, Fasl, Socs3, Lag3, Btla, Pdcd1* and *Ifng* **(Figs. 5I-J)**, along with increased MHC expression, indicating activation but also strong inhibition **(Fig. 5K)**.

Importantly, ICI treatment caused excessive pro-inflammatory cytokine production in both $CD4^+$ T cells and tumor cells, indicative of a 'cytokine storm'**(fig. S8C-D)**.

Quadruple treatment led to upregulation of *Itgae, Gzmk, Cd28, Tbx21, Itga1, Tnf* and *Tnfrsf9*, associated with T cell activation and effector functions **(Figs. 5I-J)**, and increased MHC molecule expression for effective antigen presentation, without causing the upregulation of multiple chemokines and cytokines **(Fig. 7K, fig. S8C-D)**.

In conclusion, dysregulation of $CD4^+$ and $CD8^+$ T_{eff} cells, expansion of T_{reg} cells, and downregulation of MHC gene expression and antigen presentation confer BRAFi+MEKi therapy resistance. ICI treatment alone resulted in partial activation but also a cytokine storm. The survival benefit of combining ICI even in BRAFi+MEKi-resistant murine $BRAF^{V600E}$ HGG **(Table S3)** is achieved only with quadruple treatment, which ensures full activation of $CD4^+$ and $CD8^+$ T cells without excessive cytokine production.

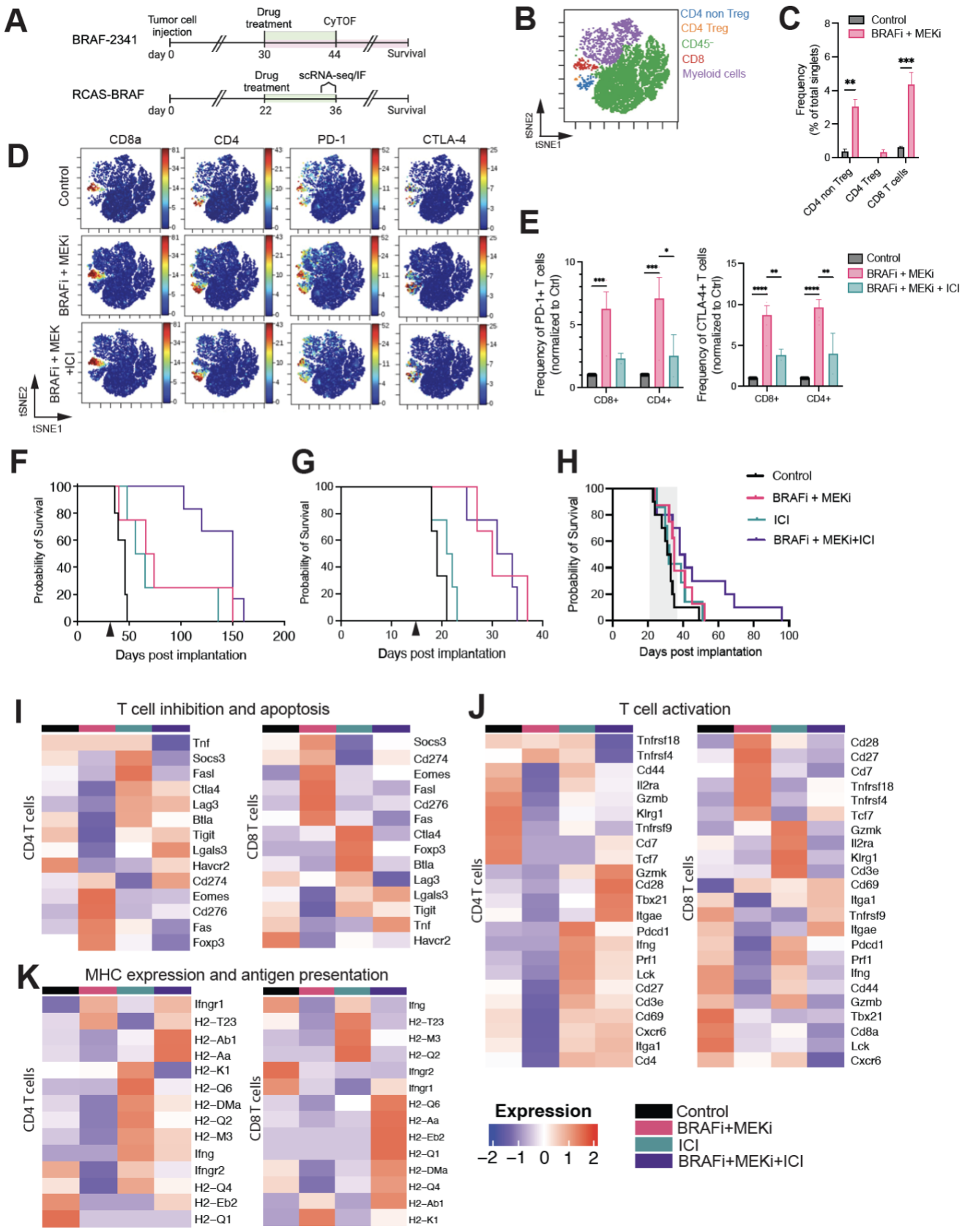
A
BRAF-2341
Tumor cell injection
Drug treatment
CyTOF
day 0
30
44
Survival
RCAS-BRAF
Drug treatment
scRNA-seq/IF
day 0
22
36
Survival
B
CD4 non Treg
CD4 Treg
CD45⁻
CD8
Myeloid cells
tSNE2
tSNE1
C
Control
BRAFi + MEKi
Frequency (% of total singlets)
CD4 non Treg
CD4 Treg
CD8 T cells
D
CD8a
CD4
PD-1
CTLA-4
Control
BRAFi + MEKi
BRAFi + MEK +ICI
tSNE2
tSNE1
E
Frequency of PD-1+ T cells (normalized to Ctrl)
Frequency of CTLA-4+ T cells (normalized to Ctrl)
CD8+
CD4+
Control
BRAFi + MEKi
BRAFi + MEKi + ICI
F
Probability of Survival
Days post implantation
G
Probability of Survival
Days post implantation
H
Probability of Survival
Days post implantation
Control
BRAFi + MEKi
ICI
BRAFi + MEKi+ICI
I
T cell inhibition and apoptosis
CD4 T cells
Tnf
Socs3
Fasl
Ctla4
Lag3
Btla
Tigit
Lgals3
Havcr2
Cd274
Eomes
Cd276
Fas
Foxp3
CD8 T cells
Socs3
Cd274
Eomes
Fasl
Cd276
Fas
Ctla4
Foxp3
Btla
Lag3
Lgals3
Tigit
Tnf
Havcr2
J
T cell activation
CD4 T cells
Tnfrsf18
Tnfrsf4
Cd44
Il2ra
Gzmb
Klrg1
Tnfrsf9
Cd7
Tcf7
Gzmk
Cd28
Tbx21
Itgae
Pdcd1
Ifng
Prf1
Lck
Cd27
Cd3e
Cd69
Cxcr6
Itga1
Cd4
CD8 T cells
Cd28
Cd27
Cd7
Tnfrsf18
Tnfrsf4
Tcf7
Gzmk
Il2ra
Klrg1
Cd3e
Cd69
Itga1
Tnfrsf9
Itgae
Pdcd1
Prf1
Ifng
Cd44
Gzmb
Tbx21
Cd8a
Lck
Cxcr6
K
MHC expression and antigen presentation
CD4 T cells
Ifngr1
H2–T23
H2–Ab1
H2–Aa
H2–K1
H2–Q6
H2–DMa
H2–Q2
H2–M3
Ifng
Ifngr2
H2–Q4
H2–Eb2
H2–Q1
CD8 T cells
Ifng
H2–T23
H2–M3
H2–Q2
Ifngr2
Ifngr1
H2–Q6
H2–Aa
H2–Eb2
H2–Q1
H2–DMa
H2–Q4
H2–Ab1
H2–K1
Expression
−2 −1 0 1 2
Control
BRAFi+MEKi
ICI
BRAFi+MEKi+ICI

511

Figure 5. BRAFi+MEKi Enhanced Anti-tumor Effects and T cell Activation of Immune Checkpoint Inhibition

(A) Experimental timeline (green: 14 days treatment for CyTOF and scRNA-seq analyses; pink: continuous treatment for survival analysis) in BRAF-2341 and RCAS-BRAF HGG mouse models.

(B) Representative t-distributed stochastic neighbor embedding (tSNE) map of cell populations from CyTOF analysis.

(C) Frequency of populations of the indicated tumor-infiltrating lymphocytes in control and BRAFi+MEKi-treated tumors as determined by CyTOF analyses. Three mice per group and two biological replicates were analyzed. **P<0.01, ***P<0.001 as determined by 2-way ANOVA with Sidak's multiple comparisons test.

(D) Representative CyTOF tSNE plots depicting the relative expression levels of CD8a, CD4, PD-1 and CTLA-4 of BRAF-2341 HGG from the control and treatment groups.

(E) Graphs depicting the frequency of PD-1^+CD8^+ and PD-1^+CD4^+ (left) or CTLA-4^+CD8^+ and CTLA-4^+CD4^+ (right) T cells normalized to control. Data representative of two independent experiments and three mice/group. *****P<0.05, **P<0.01, ***P<0.001, ****P<0.0001 as determined by 2-way ANOVA with Tukey's multiple comparisons test.

(F) Kaplan-Meier survival curve of syngeneic, orthotopic BRAF-2341 HGG-bearing mice of all four treatment groups, control (vehicle, DMSO), BRAFi+MEKi, α-PD-L1 and α-CTLA-4 (ICI), and quadruple treatment (BRAFi+MEKi+ICI). The black arrow indicates the treatment initiation at day 30 post-injection. Data representative of two independent experiments and 5-6 mice/group.

(G) Kaplan-Meier survival curve in immunocompromised (athymic) mice with orthotopic BRAF-2341 tumor cells treated with BRAFi+MEKi and/or α-PD-L1 and α-CTLA-4 (ICI). Black arrow

indicates the treatment initiation at day 14 post-injection. Data representative of two independent experiments and 5-6 mice/group.

(H) Kaplan-Meier survival curve in immunocompetent C57Bl/6 mice with orthotopic $BRAF^{V600E}$ HGG (RCAS-BRAF) treated with BRAFi+MEKi and/or α-PD-L1 and α-CTLA-4 (ICI) for 14 days. The shaded area indicates the treatment period from day 22 to day 36 post-injection. Data representative of two independent experiments and 7-10 mice/group.

(I) Heatmaps of selected transcripts associated with T cell inhibition and apoptosis in CD4 and CD8 T cells in orthotopic $BRAF^{V600E}$ HGG (RCAS-BRAF).

(J) Heatmaps of selected transcripts associated with T cell activation in CD4 and CD8 T cells in orthotopic $BRAF^{V600E}$ HGG (RCAS-BRAF).

(K) Heatmaps of selected MHC transcripts associated with antigen presentation in CD4 and CD8 T cells in orthotopic $BRAF^{V600E}$ HGG (RCAS-BRAF).

PD-L1 Expression Is Elevated in BRAF-mutant HGG and GBM

PD-L1 expression was confirmed with a varied frequency score in tumor specimens from six additional patients with distinct histopathological types of $BRAF^{V600E}$ mutant gliomas, including ganglioglioma, pleomorphic xanthoastrocytoma (PXA), and malignant astrocytoma/glioma using immunohistochemistry **(Fig. 6A; Table S5)**. In addition to its high incidence in children and in these lower-grade glioma subtypes, $BRAF^{V600E}$ mutations are also present in 1-5% of adult patients with GBM [12, 13]. We therefore next assessed PD-L1 expression in a large patient cohort to provide additional rationale for considering combined BRAFi+MEKi and anti-PD-1/PD-L1 immune checkpoint inhibition in a clinical setting.

Given that PD-L1 is a potential biomarker of response to PD-1//PD-L1 ICI [54], we evaluated the association between PD-L1 expression and BRAF mutation status in a large cohort of adult GBM (IDH-wildtype) specimens (n=3126), undergoing next generation DNA sequencing, whole transcriptome sequencing, fusion profiling, MGMT pyrosequencing, and PD-L1 IHC analysis at Caris Life Sciences. BRAF mutations were categorized into five groups: Class I (V600E; 2) Class II (non-V600E with RAS-independent signaling), Class III (non-V600E with RAS-dependent signaling), activating BRAF fusion, and variants of uncertain significance (VUS). Patients with BRAF VUS (n=24) were excluded from further analysis. Compared to BRAF-wildtype GBM patients (n=3043), those with BRAF-mutant/fused tumors (n=59) were younger (54 vs. 59 years, $P=3.5x10^{-3}$), and likelier to be MGMT-unmethylated (75% vs. 56%, $P=2.1x10^{10}$). PD-L1 IHC was performed using the SP142 clone and in compliance with Clinical Laboratory Improvement Amendments (CLIA) and Internal Organization for Standardization (ISO) requirements. 54% of BRAF-mutant GBM were positive for PD-L1 protein expression, compared to just 17% of BRAF-wildtype GBM ($P<0.001$) **(Fig. 6B)**. This was orthogonally validated using

RNA expression data from samples with whole-transcriptome sequencing data available for analysis, where CD274 expression was significantly elevated in BRAF-mutated (n=17) versus BRAF-wildtype (n=1022) GBM (P=0.045) **(Fig. 6C).**

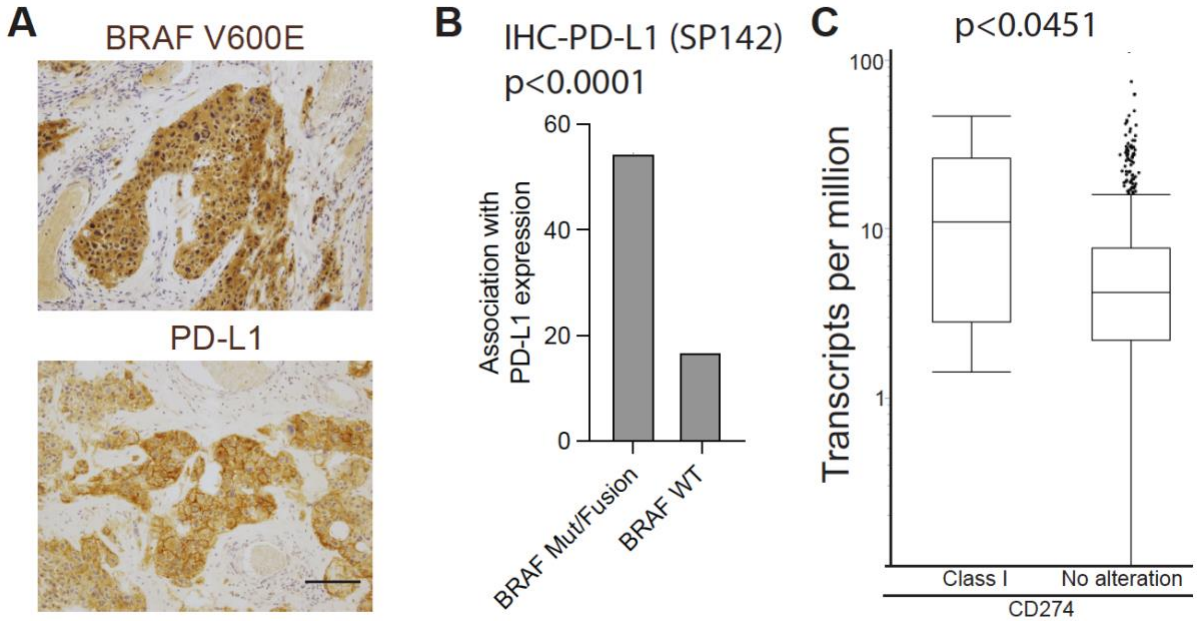

Figure 6. PD-L1 Expression in BRAF-mutant HGG and GMB is Frequent

(A) Representative IHC images for $BRAF^{V600E}$ and PD-L1 in $BRAF^{V600E}$-mutant HGG. Scale bar=25µm.

(B) Bar graph depicting percentage of patients with PD-L1 positivity in the BRAF mutation/fusion versus BRAF wildtype (no alterations) groups by IHC analysis. Clone SP142 was used for the IHC. P<0,0001; n=59 patients BRAF mut/fus and 3126 total patients.

(C) Box plot representing *CD274* (*PD-L1*) transcripts per million in the BRAF mutation/fusion (n=17) versus BRAF wildtype (no alterations; n=1022) groups, determined by whole transcriptome sequencing.

PD-L1 Expression Is Further Upregulated by BRAFi+MEKi Treatment Through the Secretion of Pro-Inflammatory Cytokines and Glial Differentiation-Promoting Molecules

To understand how BRAFi+MEKi treatment induces a further increase in PD-L1 expression which helps tumor cells to escape the immune response by inhibiting T cell activity, we performed a high-throughput nELISA assay using human STN-49 and aGBM5 cell lines treated with BRAFi+MEKi for up to 13 days, mimicking the duration of *in vivo* treatments **(Fig. 7A)**. We observed significant secretion of molecules by tumor cells in response to BRAFi+MEKi at indicated time-points. These include pro-inflammatory cytokines IL-23A, IL-27, IL-32, and other factors such as Galectin-3 **(Figs. 7A-B)**. These molecules are known for creating a pro-tumorigenic environment by dampening T cell activation, expanding regulatory T cells, promoting PD-L1-mediated immune evasion, and/or enhancing glial cell differentiation **(Fig. 7F)** [55-61]. We validated our nELISA assay results with RNA-seq data, showing that these transcripts are consistently upregulated in the aGBM5 tumor cell line after 48 hours of BRAFi+MEKi treatment **(Fig. 7C)**. Galectin-3-related transcript (*LGALS3*) is downregulated with BRAFi+MEKi treatment in treatment-resistant RCAS-BRAF mice and patient 12 (**Figs. 7D-E)**, consistent with its downregulation detected with nELISA on day 13, potentially reflective of drug resistance **(Figs. 7A-B)**.

In conclusion, we observed functional BRAF mutations in 2% of adult GBM patients, over 50% of which express clinically relevant levels of PD-L1, collectively providing a rationale to evaluate BRAFi+MEKi combined with adjuvant ICI to generate more durable responses and overcome therapy resistance in BRAF-mutant HGG and GBM. Additionally, we present candidate regulators of a pro-inflammatory tumor microenvironment that could contribute to PD-L1 mediated immune evasion in response to BRAFi+MEKi treatment, highlighting future directions for therapeutic modulation of anti-tumor immunity.

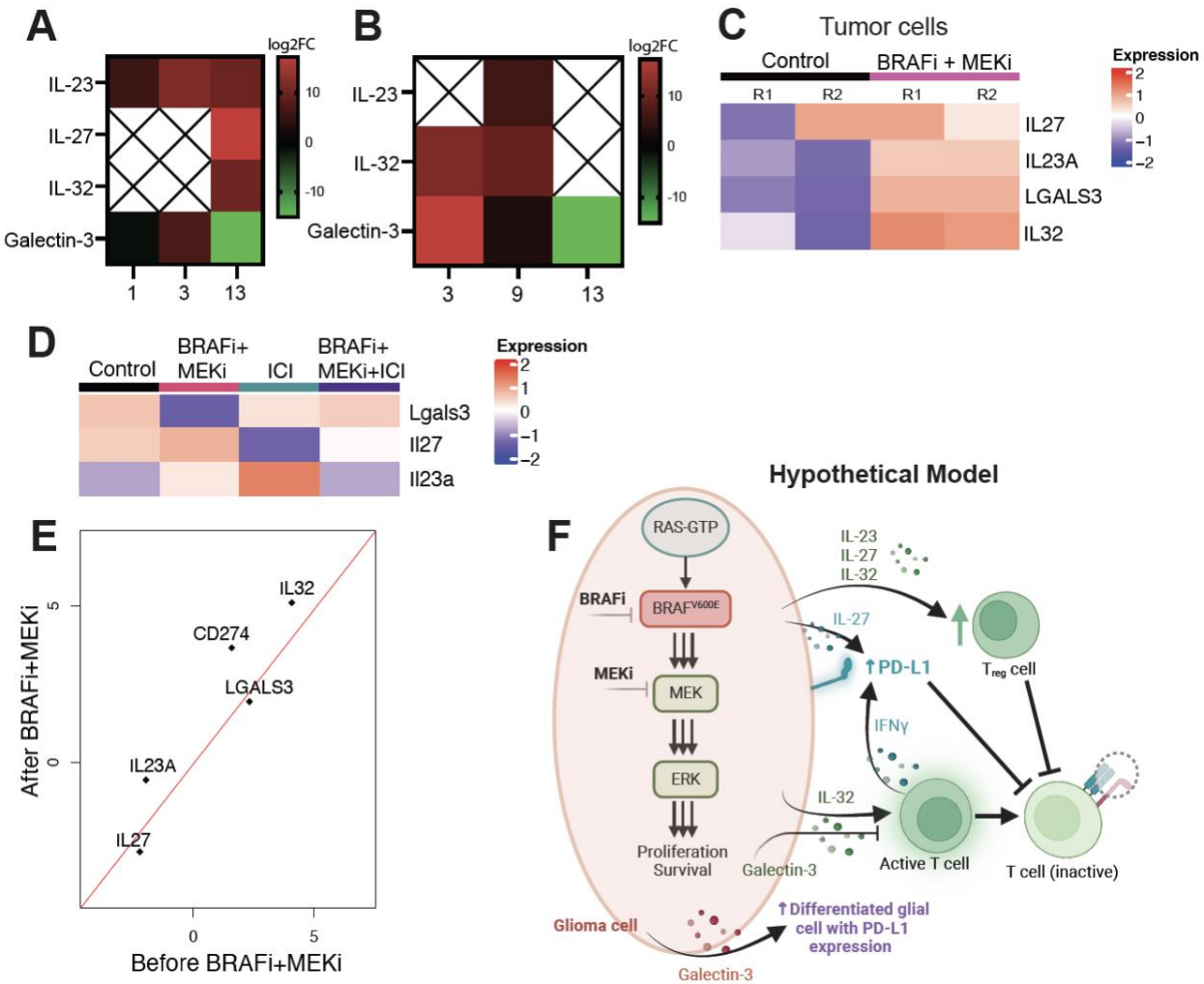

Figure 7. PD-L1 Expression is further upregulated by BRAFi+MEKi treatment through the secretion of pro-inflammatory molecules.

(A) Heatmap of secreted factors from glioma cells in response to BRAFi+MEKi treatment in the STN49 cell line. The X-axis represents days post-treatment. The color bar represents the log2 fold change (Control vs. BRAFi+MEKi) of protein expression measured by nELISA assay, with positive values indicating significantly increased expression in BRAFi+MEKi-treated group. Those with black crosses in the white boxes indicate no significant detection of proteins.

(B) Heatmap of secreted factors from glioma cells in response to BRAFi+MEKi treatment in the aGBM5 cell line. The X-axis represents days post-treatment. The color bar represents the log2 fold change (Control vs. BRAFi+MEKi) of protein expression measured by nELISA assay, with positive values indicating significantly increased expression in BRAFi+MEKi-treated group. Those with black crosses in the white boxes indicate no significant detection of proteins.

(C) Heatmap of transcripts in the aGBM5 human cell line treated with DMSO or BRAFi+MEKi for 48 hours. R stands for technical replicate.

(D) Heatmap showing the expression levels of transcripts in the RCAS-BRAF tumor cells with different treatments.

(E) The scatter plot of transcripts that are differentially expressed before and after BRAFi+MEKi treatment in patient 12.

(F) Working model of molecular mechanisms that drive BRAFi+MEKi-induced immunemodulation and glial cell differentiation.

DISCUSSION

A better understanding of how BRAFi+MEKi affects HGG cells and the HGG microenvironment is a necessary step to unravel the causes for therapy resistance and eventually find strategies to overcome it. Reported resistance mechanisms to BRAFi in HGG include reactivation of MAPK signaling, e.g., through loss of NF1 [62], and activation of receptor tyrosine kinase (RTK) [63], and MAPK pathway-independent mechanisms, such as PI3K/AKT [19, 62, 63] or autophagy [64]. Hence, preclinical studies aimed at enhancing the anti-tumor effects of BRAFi in HGG from our lab and others include combining $BRAF^{V600E}$ inhibitors with cdk4/6 inhibitor PD0332991 [65], radiation[66], polo-like-kinase-1 (PLK1) inhibitor [44], MEK inhibitor AZD6224 + mTOR inhibitor everolimus [67], EGFR inhibitor HKI-272 [63], and autophagy inhibitor hydroxychloroquine [64, 68, 69]. Few combinations have however progressed to clinical trials (NCT04201457, NCT03919071).

Our new data point to lineage-specific adaptive BRAFi+MEKi resistance mechanisms in $BRAF^{V600E}$ HGG, involving both tumor cell-intrinsic and immune modulatory mechanisms. Our findings that BRAFi+MEKi treatment alters the differentiation states of both human and murine $BRAF^{V600E}$ HGG, with durable upregulation of glial differentiation signatures at the expense of oligodendrocyte progenitor cells (OPC) **(Figs. 1, 3, and fig. S4)**, could indicate a cell-state shift from proliferative to less-proliferative cells. This could potentially be mediated by the secretion of Galectin-3 from tumor cells, as revealed by our nELISA assay experiment. Galectin-3 has been implicated in oligodendrocyte differentiation with an increase in MBP expression [60, 70]. Our data further suggest that BRAFi+MEKi could effectively restore the capacity for glial differentiation that is impaired by $BRAF^{V600E}$ expression, as we showed earlier [45]. Intriguingly, whether these differentiated glial cells from glioma maintain normal physiological functions after

dual MAPK inhibition remains uncertain since both astrocytes and oligodendrocytes have been implicated in modulating immune responses and inflammation within the CNS [71, 72]. These glial cells participate in immunomodulation in diseases like multiple sclerosis by modulating innate and adaptive immune cell recruitment, infiltration, and activation through the production of cytokines, chemokines and cell adhesion molecules [71, 72]. For example, oligodendrocyte progenitor cells (OPCs) after inflammatory demyelination, or exposure to cytokines such as IFNγ, IL1β and TNFα, possess the capacity to present antigens to cytotoxic CD8 T cells [73], phagocytose myelin, and act as antigen-presenting cells to activate effector CD4 T cells [74]. Reactive astrocytes similarly regulate T-cell responses and antigen presentation [75, 76]. These studies highlight oligodendroglia and astrocytes' roles in CNS immune regulation and could suggest avenues for therapeutic exploration not only in demyelinating diseases but also in gliomas. As a result, the involvement of OPCs, oligodendrocytes and astrocytes in antigen presentation and immune targeting may have relevance. The potential interplay among glioma, immune cells and glial cells is suggested by our discovery that the immune checkpoint molecule PD-L1 is highly expressed on differentiated oligodendrocytes **(fig. S7B)** [75], which could indicate that BRAFi+MEKi deactivates T cells through generating differentiated cells.

MAPK signaling plays multiple roles in the mammalian brain, including in glial cell differentiation [77] and myelin maintenance [78, 79]. Therefore, intrinsic resistance mechanisms, such as MAPK pathway reactivation, could direct glioma cells to adopt a more differentiated phenotype resembling astrocytes and oligodendrocytes. In support of this, we see an upregulation of MAPK signaling with BRAFi+MEKi treatment in murine HGG cells (data not shown).

NESTIN^{+} HGG cells, initially sensitive **(Figs. 3B-F)**, accumulate under therapeutic pressure by BRAFi+MEKi **(Figs. 1, 3H and fig. S4)**, suggesting adaptive resistance of a cancer stem cell population. The decrease in OPC marker expression and stable or increased expression of NESTIN is also aligned with our previous findings that OPC-like BRAF^{V600E} HGG cells are more sensitive to the anti-proliferative and pro-apoptotic effects of BRAFi than their stem-like counterpart [44]. CD133/PROM1 is a marker for both cancer stem cells and differentiating oligodendrocytes [80, 81], which could explain why its expression levels remain unchanged with BRAFi+MEKi, except after long-term treatment in patient 12 **(Fig. 1C)**. The data could also indicate that there are distinct cancer stem cell populations.

BRAF and MEK inhibitors profoundly alter the tumor immune infiltrate in metastatic melanoma by enhancing antigen presentation and immune response [40, 41, 82, 83]. Our study showed that mouse models respond differently to BRAFi+MEKi treatment, with BRAF-2341 being more drug-sensitive than RCAS-BRAF **(Fig. 5)**. In BRAFi+MEKi-responsive glioma (BRAF-2341), a significant increase in CD4 and CD8 T cells accompanied by upregulated PD-L1 and IFN signaling indicates an initial anti-tumor immune response followed by T-cell dysfunction. In contrast, in the drug-resistant glioma (RCAS-BRAF), transcriptomic data indicate further immunosuppression, characterized by T-cell dysfunction and exhaustion that could contribute to dampened antigen presentation and immune escape **(Fig. 5).** Moreover, we found that BRAFi+MEKi induced tumor cells to secrete IL-23, IL-27, IL-32 and Galectin-3, as shown by nELISA. IL-27 can be secreted by tumor cells and has been shown to induce PD-L1 expression on several cancer cell types such as prostate and lung cancer cells, thus providing an alternative stimulus for PD-L1 expression in tumor cells [55]. In addition, high IL-27 expression levels are

associated with metastatic cancer [84, 85], and it can also promote pro-tumorigenic activity of T_{regs} [56]. IL-23 also has a pro-tumorigenic function by stabilizing T_{reg} cell identity and Foxp3 expression, enhancing immunosuppression [57]. IL-32 can induce IFNγ expression in $CD8^+$ T cells and Foxp3 expression in $CD4^+$ T cells simultaneously [58]. Another study also demonstrated that IL-32 expression in esophageal squamous cell carcinoma has a significant association with stromal T_{reg} infiltration, indicating IL-32 positivity in tumor cells causes immunosuppression [88]. Thus, we propose a model **(Fig. 7F)** in which these secreted IL-27, IL-23 and IL-32 molecules have a crucial role in the expansion of T_{reg} cells, which is observed following BRAFi+MEKi treatment. Galectin-3 secreted by tumor cells has been shown to suppress T cell activity and trigger $CD8^+$ T cell apoptosis, consistent with our findings observed in Figure 5I, showing upregulation of *Fas* and *Fasl* expression in $CD8^+$ T cells after BRAFi+MEKi treatment in the RCAS-BRAF model [59]. Overall, these data indicate that our murine models harbor a T cell immune infiltrate with inhibitory signals that reduce the capacity for full T cell activation and tumor-killing function even after dual BRAF and MEK inhibition. Furthermore, the aforementioned candidate molecules could potentially be useful targets for reversing immunosuppression in the tumor microenvironment.

ICIs have been slow to reach childhood gliomas due to perceived low T cell infiltration, a limited repertoire of neoantigens, and disappointing results with single-agent ICI in recurrent adult glioblastoma. Despite encouraging data in mouse models [31, 32], PD-1//PD-L1 immune checkpoint blockade in combination with standard treatment by chemoradiation and temozolomide showed no survival benefits in GBM [34, 89]. IFNγ is typically secreted by activated T cells and can directly upregulate the expression of MHC class I/II genes in human tumor cells [51]. IFNγ upregulates PD-L1 in murine glioma cells [90] and IFNγ levels were positively correlated with PD-L1 expression in human glioma which has clinical importance as an immunotherapy target

[91]. Abundant PD-L1+ tumor-associated macrophages and lack of MHC-II-expressing antigen-presenting cells are associated with resistance to dual PD-1/CTLA-4 checkpoint blockade in GBM patients [92, 93]. Taken together, our data suggest that BRAFi+MEKi could synergize with ICI by increasing MHC class I/II expression and antigen presentation and enhancing the intrinsic sensitivity of $BRAF^{V600E}$ HGG.

Our basic and clinical discoveries highlight that $BRAF^{V600E}$-mutant gliomas express PD-L1, suppressing anti-tumor immune responses **(Fig. 6)**, explaining their poorer prognosis than their BRAF wildtype counterparts despite higher levels of T cell infiltration but also explaining why they could be sensitive to ICI of the PD1//PD-L1 checkpoint.

A limitation of our study is that we only had material from two patients before and after BRAFi+MEKi. The rarity of $BRAF^{V600E}$ HGG and the lack of surgical tissue from tumors after treatment is an important hurdle in the field. Future efforts should be directed at increasing the availability of surgical samples from matched patient material before and after treatment.

While clinical trials investigating BRAFi+MEKi combination therapy with anti-PD-L1/PD-1 and anti-CLTA-4 (Ipilimumab) in $BRAF^{V600E}$ HGG are largely lacking, melanoma studies provide insights. Patients previously treated with BRAFi+MEKi showed similar outcomes when subsequently treated with PD-1 monotherapy or PD-1+Ipilimumab, and the combination of PD-1+Ipilimumab had higher toxicity compared to PD-1 alone [37]. Subsequent BRAFi+MEKi treatment after anti-PD-1 monotherapy doubled the ORR compared to anti-CTLA-4 treatment alone [94]. Additionally, BRAF wildtype patients had a high tumor control rate with anti-PD-1+MEKi, while BRAF-mutated patients had low ORR due to acquired resistance to anti-PD1+BRAFi+MEKi treatment [95]. The clinical data in metastatic melanoma highlight the

necessity of further preclinical investigation to optimize the timing of combination therapy for balancing the efficacy and toxicity of BRAFi+MEKi+ICI in HGG.

Collectively, our data provide a rationale to evaluate BRAFi+MEKi combined with adjuvant ICI to generate more durable responses and overcome therapy resistance in BRAF-mutant HGG and GBM.

Resources Availability

Lead Contact

Further information and requests for resources and reagents should be directed and will be fulfilled by the lead contact: Claudia K. Petritsch, cpetri@stanford.edu

Materials availability

Murine BRAF-M34 and RCAS-BRAF cells and patient-derived cell lines will be made available upon request and require a materials transfer agreement according to Stanford guidelines.

Data and code availability

Data supporting the findings of this study are available in the article and its supplementary files. Bulk RNA sequencing data have been deposited in NCBI's Gene Expression Omnibus (GEO) under accession number GEO: [upon acceptance of the manuscript]. Single-cell RNA sequencing data have been deposited in GEO and are accessible through GEO Series accession number [upon acceptance of the manuscript] The codes for analyzing bulk and single-cell RNA-seq data; as well as CYTOF data are available upon request. All other datasets not included within this publication are available from the corresponding author upon reasonable request. Links of all used tools are listed in the Key Resources Table.

Experimental Model and Subject Details

Animal Studies

For mouse studies male and female mice are used. All animal procedures were performed in accordance with institutional and federal guidelines (Stanford University APLAC protocol # 33633). Mice were housed in groups of three to five and maintained on a 12-hour light/dark

schedule. Food and water were available ad libitum. Compound transgenic mice were generated by crossing Cre-dependent BRAF CA with Ink4a/Arf flox/flox mice. *BRAF* $^{CA/WT}$*; Ink4a/Arf* $^{flox/flox}$ mice were of a pure FVB/N or C57Bl/6 genetic background. Littermates carrying appropriate genotype(s) were randomly assigned to experimental groups. Mice were intracranially injected postnatally or at 6-8 weeks of age. Mice were treated and analyzed at specific postnatal days or in adulthood, as indicated in the text and figure captions.

Human Studies

Tumor specimens and clinical information were collected according to protocols approved by the Research Ethics Board. Patients provided informed consent, and ethical approval was obtained from the Institutional Review Board at Stanford University and University. Formalin-fixed, paraffin-embedded (FFPE) brain tumor tissue was obtained from patients with BRAF/RAF/MAPK mutations with CDKN2A loss and IDH-mutant astrocytoma. Clinically relevant dual MAPK pathway inhibitors were administrated to a 13-year-old boy with BRAF-mutant high-grade GBM who eventually succumbed to the disease. The patient was initially treated with one cycle of doxorubicin/ifosfamide treatment with 65.20 Gy in 35 fractions radiotherapy. The patient subsequently underwent dabrafenib and trametinib (T) treatment until his death. Separate primary patient samples were also obtained from Children's Hospital Colorado (Aurora, CO) in accordance with local and federal human research protection guidelines and Institutional Review Board regulations. Clinical and pathological features of patient 12 with BRAF-mutant glioma were described in Schreck et al [62]. Specifically, this young adult man diagnosed with high-grade GBM was initially treated with temozolomide with 60 Gy in 30 fractions radiotherapy. The patient subsequently received 6 cycles of adjuvant temozolomide for 6 months. However, given his first

local recurrence 3 months later, this patient then underwent dabrafenib and trametinib treatment for 13 months. All tumor specimens were given a sequential unique identifier to ensure complete deidentification.

For PD-L1 expression comparisons in adult GBM, clinical pathology data were obtained from 3126 glioblastoma tissue specimens profiled at Caris® Life Sciences. All samples were from adult patients (≥18 years of age). Each tumor was reviewed by board certified pathologists and classified as a glioblastoma based on World Health Organization (WHO) classification guidelines. Given changes in the WHO classification of GBM, samples with mutations in *IDH1* or *IDH2* were excluded from analyses to conform with 2021 revisions to the WHO classification of brain tumors. Tumor specimens were collected via manual microdissection and harvesting targeted tumor tissue. Next-generation sequencing was performed on genomic DNA isolated from formalin-fixed paraffin-embedded (FFPE) samples using either a custom-designed SureSelect XT assay (592 whole-gene targets, Agilent Technologies, Santa Clara, CA) or whole-exome sequencing. All variants were detected with >99% confidence based on allele frequency and amplicon coverage, with an average sequencing depth across all amplicons >500x. DNA sequencing results are validated per Clinical Laboratory Improvement Amendments (CLIA) and Internal Organization for Standardization (ISO) requirements. *MGMT*p pyrosequencing and IHC for PD-L1 (SP142 clone) was performed on all samples. ArcherPlex Fusion profiling data were available for 69% of samples, and bulk whole-transcriptome sequencing data were available for 33% of samples.

Cell Lines and Primary Cultures

All cell lines and primary cultures were maintained in humidified cell culture incubators at 37ºC under 5% CO_2. SU-aGBM5 is a BRAF V600E mutant GBM cell line from a young adult

obtained from Dr. Michelle Monje (Stanford University, CA, USA). Murine BRAF^{V600E} mutant glioma cell lines (BRAF-2341, BRAF-M34) were derived from murine glioma, induced by injection of adenovirus-Cre into the brain of *BRAF* $^{CA/WT}$*;Ink4a/Arf* $^{flox/flox}$ mice, as previously described [45]. Cells were maintained in 50% Neurobasal-A medium without L-Glutamine (10888022; ThermoFisher Scientific, Waltham, MA) and 50% D-MEM/F12 medium (11330-032; ThermoFisher Scientific), supplemented with 0.1mM MEM Non-Essential Amino Acids Solution (11140-050; ThermoFisher Scientific), 1 mM MEM Sodium Pyruvate Solution (11360-070; ThermoFisher Scientific), 1X GlutaMAX-I Supplement (35050-061; ThermoFisher Scientific) and 10 mM HEPES Buffer (15630-080; ThermoFisher Scientific). Gibco™ B27 Supplement without vitamin A (12587010; ThermoFisher Scientific) and N2 supplement (17502048; ThermoFisher Scientific) were also added to the medium. Cells were supplemented twice a week with 40 ng/ml FGF (100-146; Fujifilm Irvine Scientific, Santa Ana, CA) and EGF (100-26; Fujifilm Irvine Scientific), and 10 ng/ml PDGF-AA (100-16; Fujifilm Irvine Scientific), PDGF-BB (100-18; Fujifilm Irvine Scientific) and STEMCELL Technologies heparin (7980; ThermoFisher Scientific). M034, RCAS and aGBM5 cell lines were cultured on laminin (L2020; Sigma-Aldrich, St. Louis, MO), while STN049 grew on pol-l-ornithine (P3655; Sigma-Aldrich), following manufacturer's instructions. Lentivirus-luciferase modifications were performed as previously described [19]. Authentication of patient-derived cell lines was performed by whole exome sequencing, qRT-PCR, and DNA fingerprinting (IDEXX BioAnalytics, Westbrook, ME).

Method Details

Intracranial Injections of Adenovirus

BRaf $^{CA/WT}$*; Ink4a/Arf* $^{flox/flox}$ mice were injected with 2 µl of adenovirus expressing cre recombinase under the control of the ubiquitous CMV promoter (Ad-Cre; Titer = 1x10^10 PFU/ml; Vector

Biolabs, Malvern, PA) to induce BRaf V600E expression and deletion of tumor suppressor genes p16 ^{Ink} and p19 ^{Arf} [45]. Control mice were injected with adenovirus expressing GFP (Ad-GFP; Vector Biolabs). The stereotaxic coordinates selected to target the cortical layer, relative to bregma, are anterior-posterior–1.00 mm, medial-lateral–1.80 mm, and dorsal-ventral–2.5 mm. Animals were observed and sacrificed when exhibiting symptoms consistent with intracranial tumor formation. Brains of symptomatic mice were resected, and sectioned and tumor-bearing brains were subjected to hematoxylin and eosin (H&E) and immunofluorescence staining.

Orthotopic Glioma Generation

6-8-week-old FVB/N and nu/nu mice were used for orthotopic implantation of BRAF-2341 glioma cells, while age-matched C57Bl/6 mice were used for orthotopic implantation of BRAF-M34 glioma cells. C57Bl/6 mice at postnatal day 7 were used for orthotopic implantation of RCAS-BRAF murine glioma cells. Adult and postnatal mice were anesthetized with isoflurane inhalation (4% induction, 2% maintenance) and ice block, respectively. The head of the anesthetized mouse was fixed in a stereotaxic frame using a nose cone and ear bars. Eyes were moistened with water-based lubricant and the fur was cleared over the head with an electric shaver. A sterile cotton tip soaked in betadine was used to swab and clean the surface of the incision site. A midline incision was made on the scalp and a small hole was drilled into the skull to expose the brain surface at the following stereotaxic coordinates selected to target the striatum, relative to bregma (anterior-posterior–0.00 mm, medial-lateral–2.00 mm). Cells were gently drawn up into a blunt-tipped 26G needle attached to a 10µl syringe (Hamilton Company, Reno, NV). The syringe was then placed into a microinjection pump (UltraMicroPump III, World Precision Instruments, Sarasota, FL) attached to the stereotaxic frame and lowered slowly into the injection site at a depth of 3 mm for adult mice and 1 mm for postnatal mice. The microinjection pump controlled the injection of cells

at a flow rate of 0.5µl/min, after which the needle was left in place for 5 mins to ensure complete diffusion of cells and avoid backflow. Following the slow withdrawal of the needle, the hole was closed with dental cement, the incision was sutured, and mice were observed until full recovery from anesthesia on a heated surface. Mice were monitored weekly. Animals assessed for survival were monitored until they lost more than 15% of their original body weight and/or had clinical symptoms of tumor development (hydrocephalus, lethargy, hunched posture). BRAF-2341 and BRAF-M34 displayed characteristics of HGG, such as hypercellular proliferation of atypical glial cells, focal necrosis, high microvascular proliferation, and occasional mitotic figures. RCAS-BRAF showed consistent and invasive growth into various brain regions, including the ipsilateral hippocampus, thalamus, white matter, lateral septal complex, somatomotor isocortex, and contralateral hemisphere **(figs. S2I)**. Histologically, RCAS-BRAF tumors exhibited hypercellular proliferation of malignant ovoid to spindled cells arranged in fascicles and sheets, with lower necrosis and microvascular proliferation compared to BRAF-2341 and BRAF-M34 **(Fig. 2I, fig. S2I, table S2)**.

Drug Preparation and Treatment

Dabrafenib (cat#2807; Selleckchem, Houston, TX) and Trametinib (cat#S2673; Selleckchem) were dissolved in DMSO at a concentration of 10 mg/ml and 2 mg/ml, respectively, and stored at -20°C. For *in vivo* experiments, a fresh solution of the drug was prepared on each treatment day, by thawing the stock solution in a warm water bath and diluting it in an aqueous mix of 0.5% hydroxypropyl methylcellulose (HPMC) and 0.2% tween solution to a final concentration of 30 mg/kg dabrafenib and 1 mg/kg trametinib combined in 200 µl/animal. Drugs were delivered by oral gavage once daily. For survival analysis, dabrafenib was given at 2.5mg/kg daily by oral gavage. Trametinib was given at 1mg/kg daily by oral gavage. BioXCell anti-PD-L1 (clone

10F.9G2; ThermoFisher Scientific) was given at 20 mg/kg i.p. at day 1 and 8 mg/kg every 2 days thereafter, BioXCell anti-CTLA-4 (clone 9D9; ThermoFisher Scientific) was given at 8 mg/kg i.p. at day 1 and 2 mg/kg every 2 days thereafter.

For *in vitro* experiments, stock solutions of dabrafenib and trametinib were dissolved at 10 mM concentration in DMSO (3176-100 ml; ThermoFisher Scientific,), aliquoted and stored at -80 ºC. For measuring viability and constructing dose-response curves, cells were dissociated with Accutase (NC9389010; ThermoFisher Scientific,) and 10^4 cells were plated per well in a 96-well half-white plates (3688; ThermoFisher Scientific,) using the corresponding vessel. After 24 hours, a serial dilution of 10 μM dabrafenib or trametinib were added in triplicate to the seeded cells. After 72 hours, the cell viability was measured with CellTiter-Glo® Luminescent Cell Viability Assay (G7570; Promega, Madison, WI). Percentage of surviving cells (normalized to DMSO control) was plotted as a function of log10 drug concentration. The sigmoidal curves were generated with GraphPad Prism software (GraphPad Prism version 10.0.0, GraphPad Software, Boston, Massachusetts USA, www.graphpad.com), whereby the IC50 concentrations were calculated.

Magnetic Resonance Imaging

All MR studies were performed at 7T Bruker BioSpec system (Bruker, Billeria, MA) equipped with BGA-12S gradient insert and interfaced to ParaVision 360 V. 3.5. A 4-element receive-only mouse CryoProbe™ and 86mm volume coil were used for MR imaging. Gadobutrol solution (Gadavist; diluted 1:10 with saline; Bayer, Whippany, NJ) was administered intraperitoneally before MRI. Animals were anesthetized with 2.5% isoflurane mixed in air and O_2 and maintained with 1-1.5% isoflurane during the imaging procedure. Core body temperature was maintained at

37°C using a warm water circulator pad and a temperature controller (ThermoFisher Scientific). The animal's respiration was also monitored via pneumatic pad placed under the animal (SA Instruments, Inc., Stony Brook, NY). T2w Turbo RARE sequence was used to obtain coronal (TR/TE = 2000/30 ms, FOV = 20 x 20 mm^2, matrix = 256 x 256, slice thickness = 0.5 mm, RARE Factor = 4, NEX = 2, scan time = 4 min 16 sec) and transverse (TR/TE = 2500/30 ms, FOV = 20 x 20 mm^2, matrix = 256 x 256, slice thickness = 0.5 mm, RARE Factor = 4, NEX = 2, scan time = 5 min 20 sec) structural MRI.

Tissue Collection and Processing of Mouse Samples

Mice were intraperitoneally injected with ketamine (100mg/kg) and xylazine (10mg/kg) to induce deep anesthesia and subsequently transcardiac perfusion was performed first with phosphate-buffered saline followed by 4% paraformaldehyde (PFA)/PBS or 10% neutral buffered formalin. Brains perfused with 4% PFA were then resected, post-fixed in 4% PFA/PBS for 2 hours on ice, cryoprotected in 15% sucrose/PBS for 24 hours and then 30% sucrose/PBS for at least 48 hours, followed by embedding in Tissue-Tek® O.C.T. Compound (Sakura Finetek USA, Inc., Torrance, CA). The embedded tissues were stored at -80 ºC until sectioned. 10µm-thick coronal sections of the brain were cut on a cryostat (Leica, Wetzlar, Germany), collected onto Superfrost Plus slides (Menzel Glaser, VWR) and air dried for 1h before storing at -80ºC until stained. Brains perfused with 10% formalin were post-fixed in 10% formalin for 24 hours at room temperature, then dehydrated in 70% ethanol. They were then embedded in paraffin and sectioned using Histo-Tech protocols (Histo-Tec Laboratory Inc., Hayward, CA; http://histoteclab.com/).

Immunofluorescence Staining on Frozen Tissue Sections of Mouse and Human Samples

Frozen 10µm sections on Fisherbrand™ Superfrost™ Plus Microscope Slides (ThermoFisher Scientific) slides were washed briefly in PBS and blocked with PBS containing 0.3% Triton X-100, 5~10% normal donkey serum, and/or normal goat serum for 1 hr at room temperature (RT). The sections were then incubated with primary antibodies at RT overnight in a humidified chamber, washed briefly in PBS three times next day, followed by 1h incubation at RT with secondary antibodies, the slides were then washed three times with PBS, and cover slipped with a DAPI-containing mounting solution (VectaShield H20002; Vector Laboratories, Newark, CA) or SouthernBiotech™ Dapi-Fluoromount-G™ Clear Mounting Media; ThermoFisher Scientific) and subjected to fluorescence and confocal microscopic analysis. For multiplex immunofluorescence, some primary antibodies were incubated simultaneously. The following primary antibodies were used: chicken anti-Nestin (ab134017; Abcam, Waltham, MA), chicken anti-GFP (600-901-215; Rockland Immunochemicals, Pottstown, PA), goat anti-PDGFRα (AF1062; R&D Systems, Minneapolis, MN), mouse anti-NeuN (MAB377; Millipore Sigma, Burlington, MA), mouse anti-PD-L1 (329702; BioLegend, San Diego, CA), rabbit anti-Olig2 (AB9610; Millipore Sigma, Burlington, MA), rabbit anti-Ki67 (ab15580; Abcam), rat anti-CD133 (14-1331-82; ThermoFisher Scientific), rat anti-GFAP (13-0300; ThermoFisher Scientific), rat anti-MBP (ab7349; Abcam), rat anti-CD8a (50-112-9493; ThermoFisher Scientific) and rat anti-CD4 (100402; BioLegend). Secondary antibodies raised in donkey or goat and conjugated to Alexa Fluor 488, Alexa Fluor 555, Alexa Fluor 594, Alexa Fluor 647, or Alexa Fluor 790 were purchased from Jackson ImmunoResearch Labs (West Grove, PA) or Invitrogen (now ThermoFisher Scientific) and used at 1:200 dilution. Secondary antibodies raised in donkey or goat and conjugated to Alexa Fluor 488, Alexa Fluor 555, Alexa Fluor 594, Alexa Fluor 647, or Alexa Fluor 790 were purchased from

Jackson ImmunoResearch Labs (West Grove, PA) or Invitrogen (now ThermoFisher Scientific) and used at 1:200 dilution.

Hematoxylin & Eosin Staining, Immunohistochemistry and Bulk RNA Sequencing

Patient tissue was processed according to well-established histologic protocols, including fixation in 10% neutral buffered formalin, paraffin embedding, sectioning (5μm), and standard histochemical staining using hematoxylin and eosin (H&E). Comprehensive diagnostic evaluation included review by a board-certified pathologist specialized in anatomic pathology and neuropathology, as well as a senior fellow in neuropathology. Immunohistochemical staining of patient tumor tissue was performed using antibodies BRAF V600E (clone VE; 790-5095; Roche Diagnostics, Indianapolis, IN), PD-L1 (clone SP142) with the 3,3'-diaminobenzidine (DAB) chromogen. Immunohistochemical staining of RCAS-BRAF mouse brain sections was performed by Histo-Tec. For bulk RNA sequencing, RNA extraction from paired FFPE-preserved specimens from patient 12, library preparation, and RNA sequencing were performed as previously described in Schreck et al [62].

Differentiation Assays

Differentiation assays were performed as previously published [46] with minor modifications. Dissociated cells were plated in Lab-Tek II CC^2 chamber slides (154941; ThermoFisher Scientific) coated with 10 ug/ml laminin or 0.01% poly-l-ornithine at 3 x 10^4 cells per well. Two different growth conditions were used for this assay: medium without growth factors and medium supplemented with 60 nM triiodothyronine (T3; Millipore Sigma) and 10 ng/mL CNTF (Peprotech, Cranbury, NJ), termed as “differentiation” medium. Fresh medium and drugs (0.7 μM

dabrafenib and 0.3 μM trametinib) was added every 3 days, for promoting oligodendrocyte differentiation. The duration of the treatment was 13 days, and the experiment was performed in two technical replicates. Cells were fixed with 4 % PFA (EMD) for 10 min at RT and stained with primary antibodies overnight and secondary antibodies for 1 hour before being mounted in Vectashield mounting medium.

nELISA Assay

The high-plex secretome was profiled by NomicBio (https://nomic.bio/), which is offered as a service by the company. However, this platform does not detect mouse targets. For this study, secreted cytokines from the human cell lines (STN049 and aGBM5) were screened with the nELISA platform (https://doi.org/10.1101/2023.04.17.535914). Briefly, cells from STN049 and aGBM5 were dissociated using Accutase and 10^4 cells per well were seeded in 96-well plates (Fischer Scientific, 7200309). For this experiment, three different medium conditions were used (medium supplemented with/without growth factors and differentiation medium (see Differentiation Assay)). In addition, the medium was supplemented with dabrafenib and trametinib (0.7 μM and 0.3 μM, respectively) or DMSO (10 μM) as a control. 50 μl of medium from each culturing/drug combination was collected in triplicate on day 1, 3, 9 and 13 post-therapy and at the time fresh medium was added to the cells. Finally, frozen medium containing cells' secreted cytokines and control medium (freshly prepared without cell culturing) was submitted for nELISA measurements. For data analysis, nELISA signals were first normalized by their respective well conditions without cells. The signal matrix was then normalized using normalizeBetweenArrays(), a function from the limma Bioconductor package, which normalizes expression intensities so that the intensities or log-ratios have similar distributions across a set of arrays. Heatmaps for proteins

of interest were generated by calculating the log2 fold change of protein expression per day and plotting across time with GraphPad Prism software (GraphPad Prism version 10.0.0, GraphPad Software, Boston, Massachusetts USA, www.graphpad.com).

Immunocytochemistry

Prior to staining, the cells were permeabilized with 0.25% Triton-X in PBS ($Ca^{2+/}Mg^{2+}$) for 5 minutes at room temperature, washed with PBS and blocked with 10 % normal donkey serum for (NC9624464; ThermoFisher Scientific) for 1 hour at room temperature on a gentle shaker. After this step, the blocking solution was aspirated and 150 µl of primary antibody solution was added to each well: chicken anti-human/mouse Nestin, 1:200 (ab134017; Abcam), goat anti-human/mouse Olig2, 1:200 (AF2418; R&D Systems), rat anti-mouse PD-L1(1:50; A14764; ThermoFisher Scientific), mouse anti-human PD-L1 1:50 (329702; BioLegend), rat anti-human/mouse MBP 1:100 (ab7349; Abcam) and DAPI 1:1000 (NC1848444; ThermoFisher Scientific). The primary antibodies were incubated overnight at 4ºC on a gentle shaker. On the next day, the primary antibody solution was aspirated, and the wells were washed twice with PBS, which was followed by 150 µl of secondary antibody staining solution: donkey anti-chicken-488, donkey anti-goat-647, goat anti-rat-488, goat anti-mouse-594. After 1 hour of incubation, the cells were washed twice with PBS and mounted in Vectashield mounting medium.

Confocal imaging and image processing

Stained 10µm thick coronal sections and cultured cells in chamber slides were imaged by laser scanning confocal microscopy (Zeiss LSM980) which was used to detect up to five fluorophores

by laser excitation at 405, 488, 561, 639, and 730 nm wavelengths. Confocal images were acquired using a 20X objective. Images were imported into Fiji image analysis software for quantification of cellular density and fluorescence intensity in the regions of interest. All analyses were performed in a blinded fashion.

Flow Cytometry and MACS

Mouse brains with BRAF-2341 tumor cells were resected, and single cell dissociates were obtained using 15 units/ml of Papain for 30 min at 37ºC, and tissue was dissociated using a P1000 pipette, strained through a 70 µm cell strainer over a 50 ml conical tube at room temperature. Cells were washed in 10 ml of ice-cold, sterile 1 x phosphate-buffered saline (PBS, Ca2+, Mg2+-free) and centrifuged at 1300 rpm for 10 min at 4ºC. For flow cytometric analyses of CD133+ and Nestin+ cell frequency, cells were resuspended using PBS (Ca2+, Mg2+-free) + 0.2 mmol/L EDTA, resuspended in FACS buffer (PBS+EDTA+0.5% BSA) at 1E6 cells/100 µl, and incubated with primary antibodies, which were chicken anti-Nestin (1:100; ab134017; abcam) + goat anti-chicken-488 (1:500; ab150169; abcam) and Prominin-1 biotin (1:100; 130-101-996; Miltenyi Biotec, San Jose, CA) + streptavidin-APC (1:500; 130-090-856; Miltenyi Biotec). Isotype IgG and single-channel antibodies were used as a control. Primary antibodies were incubated for 30 min on ice in the dark. Cells were washed twice in 1 ml of ice-cold 2% fetal bovine serum + PBS, secondary antibodies were added for 15 min, washed, and cells were resuspended in a FACS buffer containing Hoechst and strained immediately prior to analyses. Cells were analyzed by flow cytometry using the BD FACSCalibur™ (BD Biosciences, Franklin Lakes, NJ). The gating strategy for analyzing CD133 and Nestin positive cells involved multiple steps, including initial quality control gating to remove debris and dead cells based on their size and granularity (FSC-A vs. SSC-A), doublet discrimination (FSC-A vs. FSC-H) to exclude cell doublets and clumps,

live/dead discrimination (PI or DAPI), and specific gating for CD133 and Nestin positive cells based on unstained controls and isotype controls that can help set the appropriate threshold for positivity. Raw data was processed and analyzed with the FlowJo™ software (10.7.1; BD Biosciences).

Magnetic sorting was performed as described [46] according to manufacturer's instructions, with the modification that 10^7 cells were resuspended in 60 ml of ice-cold MACS buffer solution, incubated in 20 µl of FcR blocking reagent for 10 min at 2-8ºC, 20 µl of anti-A2B5 (130-123-953; Miltenyi Biotec,) were added per 10^7 cells, and incubated at 2-8ºC for 15 min. Cells were washed twice and passed onto a LS column in an OctoMACS™ separator (Miltenyi Biotec). Columns were washed three times with 500 ml of MACS buffer and placed in a collection tube. A2B5$^+$ cells were collected by firmly pushing the plunger into the column, and immediately used for RNA extraction.

Mass Cytometry and Analyses

FVB/N mice injected with BRAF-2341 glioma cells were treated as indicated for 2 weeks. Tumor cells were isolated and subjected to mass cytometry (CyTOF) utilizing a 42-antibody panel (Weiss UCSF Mouse Neural tumor CyTOF Antibody Panel). 1 ml of 1X Barcode Perm Buffer (Fluidigm) was added to isolated tumor cells, spun at 600x g for 5 minutes, vacuum aspirated to ~50 µl and 750 µl 1X Barcode Perm Buffer was added again to cells. 100 µl of resuspended barcode stocks (two sets of 20-plex barcodes SCAC) were added to corresponding cell tubes and mixed by pipetting. Cells were incubated for 30 minutes at room temperature on RotoMix shaker at max speed, spun down, the excess buffer was aspirated, and cells were washed three times in cell

staining media (CSM), and finally, 100 µl CSM was added to each cell tube. For each barcode pool, barcoded cells were combined and strained into appropriate 5 ml FACS tubes and the volume of pooled tubes was brought up to 5 ml with CSM. Pooled barcoded cells were spun at 600x g, for 5 minutes, the supernatant was aspirated, and cells were vortexed to disrupt pellets and resuspended at 47 µl per 1E6 cells. 2 µl mouse Fc Block (clone 2.4G2; 0.5 mg/ml) per 1E6 cells were added to each tube, stained for 30 minutes at room temperature on RotoMix shaker at max speed. Cells were washed two times in 3 ml CSM, spun at 600x g for five minutes, excess CSM was aspirated, and the pellet was vortexed for 10 seconds to disrupt the pellet. Pellets were resuspended at 35 µl per 1E6 cells. Surface antibody staining (Antibody Cocktail A) was performed first, with 15 µl of Antibody Cocktail A per 1E6 cells added and mixed by pipet. Cells stained for 30 minutes at room temperature on RotoMix shaker at max speed and washed twice in 3 ml CSM, spun down at 600x g for 5 minutes, excess liquid aspirated, and pellet disrupted by 10 second vortex. Intracellular antibody staining (Antibody Cocktail B) was performed next by adding 3 ml Perm-S Buffer (Fluidigm) to the disrupted cell pellet and incubating it on ice for 30 minutes. Barcoded cells were spun at 600x g for 5 minutes and supernatant vacuum aspirated. Cell pellets were resuspended with Perm-S Buffer (Fluidigm) at 35 µl per 1E6 cells and mixed by pipet. 15 µl of Antibody Cocktail B was added per 1E6 cells, mixed by pipet, and stained for 30 minutes at room temperature on RotoMix shaker at max speed. Cells were washed first with 3 ml Perm-S Buffer (Fluidigm), spun at 600x g for 5 minutes, supernatant aspirated, and pellet vortexed for 10 seconds and washed a second time with 3 ml CSM followed by spin, aspiration, and vortex. Cells were then resuspended in 500 µl CSM and transferred to 15 ml polypropylene conical tubes and treated with 4500 µl Ir-intercalator cocktail. Cells were stored at 4ºC overnight.

To prepare samples for CyTOF, 9 ml CSM was added per tube, cells were counted, then spun at 600x g for 5 minutes and vacuum aspiration left ~100 µl residual volume. To each tube, 800 µl MaxPar PBS (Fluidigm) was added, mixed, and transferred to an Eppendorf Protein Lo-bind 1.5 ml tube, spun at 600x g for 5 minutes, then vacuum aspirated to ~100 µl residual volume. Cells were washed twice with 1.4 ml MilliQwater, spun at 600x g for 5 minutes and vacuum aspirated to ~100 µl residual volume. The barcoded cells were then resuspended in 1 ml 1X Four-Element EQ beads (Fluidigm), strained through blue-cap FACS tubes, and cells were recounted. CyTOF was performed on 7.87E6 cells in Pool 1 and 1.23E7 cells in Pool 2. FCS files were concatenated into a single FCS file utilizing the FCS concatenation tool from Cytobank.

Data was normalized using the Premessa normalizer tool in R (https://github.com/ParkerICI/premessa). CyTOF data was debarcoded and the panels were renamed using the same Premessa tool as above in R. The normalized, debarcoded, and renamed fcs files were uploaded to Cytobank for further downstream analyses of the data, including isolation and clustering of $CD45^+$ cells with Phenograph. The fcs file containing the $CD45^+$ pool with Phenograph coordinates was downloaded from Cytobank and loaded to the Cytofkit2 ShinyAPP via R (https://github.com/JinmiaoChenLab/cytofkit2), whereby the clusters were annotated and visualized on heatmaps and t-SNE plots.

cDNA Synthesis and Quantitative PCR

Total RNA was extracted using the RNeasy Plus kit (QIAGEN) and cDNA synthesis was performed using the iScript cDNA Synthesis Kit (Biorad). Quantitative RT-PCR was run using SYBR Green PCR Master Mix (Thermo Fisher Scientific) using a cycling program of 10 min at 95ºC followed by 40 cycles of 95ºC for 15 sec and 95ºC for 60 sec. All primer sequences are available in Table S4.

RNA Sequencing and Analysis

RNA concentration was quantified by Nanodrop (Nanodrop Technologies, Wilmington, DE) and 0.4 µg of each sample was submitted to Novogene (Novogene Corporation Inc., Sacramento, CA) for RNA sample QC, library preparation and sequencing (Illumina PE150, 20M paired reads). FASTQ files were uploaded to Galaxy (usegalaxy.org), an open-source, web-based platform for sequencing analysis where we performed quality control (FastQC), mapped the reads to hg19 or mm10 reference genome (STAR aligner), counted reads per annotated gene (FeatureCounts), and determined differentially expressed features (DESeq2). Pathway enrichment analysis was performed using gene set enrichment analysis (GSEA) combined with pathway definitions from MSigDB, KEGG, and Reactome databases (clusterProfiler). GSEA was run using pre-ranked mode for all genes based on log2 fold change derived from the differential expression analysis. Pathways with a normalized enrichment score >1 or <-1 at FDR <10% were considered significant. Heatmaps were generated using the ComplexHeatmap package in R.

Single-cell Library Preparation and Sequencing

C57Bl/6 mice injected with RCAS-BRAF glioma cells were treated as indicated for 2 weeks. Brains collected after intracardiac perfusion with 20ml of PBS were dissociated into single-cell suspensions using the mouse tumor dissociation kit (#130-096-730) and the gentleMACS Octo Dissociator according to the manufacturer's protocol (Miltenyi Biotec). Single-cell libraries of dissociated single cells were prepared using the BD Rhapsody™ platform (BD Biosciences). Single-cell suspensions obtained from the brains of individual tumor-bearing mice were stained with oligonucleotide-conjugated Sample Tags using the mouse Single-Cell Multiplexing Kit (cat# 633793) following the manufacturer's protocol (BD Biosciences). Sorted live cells from barcoded samples were counted and pooled at equal ratios and loaded onto a BD Rhapsody cartridge for

capture. Cell capture and library preparation were completed using the BD Rhapsody Whole Transcriptome Analysis (WTA) Amplification Kit (cat# 633801). Briefly, cells were captured with beads in microwell plate, followed by cell lysis, bead retrieval, cDNA synthesis, template switching and Klenow extension, and library preparation following the BD Rhapsody protocol. The quality of the final libraries was assessed by using an Agilent's Bioanalyzer high sensitivity analysis and concentrations were measured by a Qubit method. The final libraries were diluted and normalized to 4nM and then pooled for paired-end sequencing on NovaSeq 6000 sequencer (Illuminia, San Diego, CA) in Novogene (Novogene Corporation Inc., Sacramento, CA).

Analysis of Single-cell RNA Sequencing Data

Rhapsody data were processed using the Seven Bridges Genomics cloud platform (San Francisco, CA) and BD Rhapsody Sequence Analysis Pipeline (v2.0) to quantify transcript levels with default parameters against the GRCm38 genome for BD Rhapsody scRNA-seq data. The plug-in Lex BDSMK was run to separate out the Sample Tags. After analysis, output files were imported into R package Seurat (version 4) for downstream clustering analysis and visualization. Briefly, cells were filtered, normalized and the top 2000 highly variable features and the top 20 principal components were selected for further clustering analysis. Fourteen clusters were identified with the default resolution, including tumor and T-cell clusters based on the expression of their specific markers. Gene Ontology (GO) pathway enrichment analysis for differentially expressed genes between groups was performed using the clusterProfiler package. For sub-clustering analysis of tumor cells, CD4 and CD8 T cells, cells from the tumor and T-cell clusters identified in primary clustering were extracted, reclustered and annotated based on subtype marker genes. Heatmaps for genes of interest were generated using the ComplexHeatmap package.

Statistical Analysis

All significance calculations were conducted using GraphPad Prism software. Statistical significance was determined using an unpaired, two-tailed Student's t-test or two-way ANOVA with Bonferroni's, Tukey's, or Sidak's multiple-comparison tests when more than two groups were being compared. Survival was analyzed by the Kaplan-Meier method using log-rank (Mantel-Cox) test. Quantitative data are reported as mean ± SEM, and any values of $P<0.05$ were considered statistically significant. *$P<0.05$, **$P<0.01$, ***$P<0.001$ and ****$P<0.0001$.

References:

1. Ostrom, Q.T., et al., *CBTRUS Statistical Report: Primary Brain and Other Central Nervous System Tumors Diagnosed in the United States in 2014-2018.* Neuro Oncol, 2021. **23**(12 Suppl 2): p. iii1-iii105.
2. Ostrom, Q.T., et al., *Alex's Lemonade Stand Foundation Infant and Childhood Primary Brain and Central Nervous System Tumors Diagnosed in the United States in 2007-2011.* Neuro Oncol, 2015. **16 Suppl 10**: p. x1-x36.
3. Lin, D., et al., *Trends in Intracranial Glioma Incidence and Mortality in the United States, 1975-2018.* Front Oncol, 2021. **11**: p. 748061.
4. Ryall, S., U. Tabori, and C. Hawkins, *A comprehensive review of paediatric low-grade diffuse glioma: pathology, molecular genetics and treatment.* Brain Tumor Pathol, 2017. **34**(2): p. 51-61.
5. Bai, X. and K.T. Flaherty, *Targeted and immunotherapies in BRAF mutant melanoma: where we stand and what to expect.* Br J Dermatol, 2021. **185**(2): p. 253-262.
6. Ribas, A. and K.T. Flaherty, *BRAF targeted therapy changes the treatment paradigm in melanoma.* Nat Rev Clin Oncol, 2011. **8**(7): p. 426-33.
7. Davies, H., et al., *Mutations of the BRAF gene in human cancer.* Nature, 2002. **417**(6892): p. 949-54.
8. Ryall, S., et al., *Integrated Molecular and Clinical Analysis of 1,000 Pediatric Low-Grade Gliomas.* Cancer Cell, 2020. **37**(4): p. 569-583 e5.
9. Mackay, A., et al., *Integrated Molecular Meta-Analysis of 1,000 Pediatric High-Grade and Diffuse Intrinsic Pontine Glioma.* Cancer Cell, 2017. **32**(4): p. 520-537 e5.
10. Mackay, A., et al., *Molecular, Pathological, Radiological, and Immune Profiling of Non-brainstem Pediatric High-Grade Glioma from the HERBY Phase II Randomized Trial.* Cancer Cell, 2018. **33**(5): p. 829-842 e5.
11. Kleinschmidt-DeMasters, B.K., et al., *Epithelioid GBMs show a high percentage of BRAF V600E mutation.* Am J Surg Pathol, 2013. **37**(5): p. 685-98.
12. Schreck, K.C., et al., *Integrated molecular and clinical analysis of BRAF-mutant glioma in adults.* NPJ Precis Oncol, 2023. **7**(1): p. 23.
13. Garber, S.T., et al., *Immune checkpoint blockade as a potential therapeutic target: surveying CNS malignancies.* Neuro Oncol, 2016. **18**(10): p. 1357-66.
14. Schindler, G., et al., *Analysis of BRAF V600E mutation in 1,320 nervous system tumors reveals high mutation frequencies in pleomorphic xanthoastrocytoma, ganglioglioma and extra-cerebellar pilocytic astrocytoma.* Acta Neuropathol, 2011. **121**(3): p. 397-405.
15. de Blank, P., et al., *Management of pediatric low-grade glioma.* Curr Opin Pediatr, 2019. **31**(1): p. 21-27.
16. Lassaletta, A., et al., *Therapeutic and Prognostic Implications of BRAF V600E in Pediatric Low-Grade Gliomas.* J Clin Oncol, 2017. **35**(25): p. 2934-2941.
17. Krishnatry, R., et al., *Clinical and treatment factors determining long-term outcomes for adult survivors of childhood low-grade glioma: A population-based study.* Cancer, 2016. **122**(8): p. 1261-9.
18. Mistry, M., et al., *BRAF mutation and CDKN2A deletion define a clinically distinct subgroup of childhood secondary high-grade glioma.* J Clin Oncol, 2015. **33**(9): p. 1015-22.
19. Grossauer, S., et al., *Concurrent MEK targeted therapy prevents MAPK pathway reactivation during BRAFV600E targeted inhibition in a novel syngeneic murine glioma model.* Oncotarget, 2016. **7**(46): p. 75839-75853.

20. Barbato, M.I., et al., *FDA Approval Summary: Dabrafenib in combination with trametinib for BRAF V600E mutation-positive low-grade glioma.* Clin Cancer Res, 2023.
21. Gouda, M.A. and V. Subbiah, *Precision oncology for BRAF-mutant cancers with BRAF and MEK inhibitors: from melanoma to tissue-agnostic therapy.* ESMO Open, 2023. **8**(2): p. 100788.
22. Gouda, M.A. and V. Subbiah, *Expanding the Benefit: Dabrafenib/Trametinib as Tissue-Agnostic Therapy for BRAF V600E-Positive Adult and Pediatric Solid Tumors.* Am Soc Clin Oncol Educ Book, 2023. **43**: p. e404770.
23. Subbiah, V., Stein, A., van den Bent, M., Wick, A., de Vos, F. Y., von Bubnoff, N., van Linde, M.E., Lai, A., Prager, G. W., Campone, M., Fasolo, A., Lopez-Martin, J. A., Kim, T. M., Hofheinz, R.D., Blay, J.Y., Cho, D.C., Gazzah, A., Pouessel, D., Yachnin, J., Boran, A., Burgess, P., Ilankumaran, P., Gasal., D., and Wen, P.Y,, *Dabrafenib plus trametinib in BRAF V600E-mutant high-grade (HGG) and low-grade glima (LGG).* Cancer Research, 2021. **81**(13).
24. Wen, P.Y., et al., *Dabrafenib plus trametinib in patients with BRAF(V600E)-mutant low-grade and high-grade glioma (ROAR): a multicentre, open-label, single-arm, phase 2, basket trial.* Lancet Oncol, 2022. **23**(1): p. 53-64.
25. Majzner, R.G., S. Heitzeneder, and C.L. Mackall, *Harnessing the Immunotherapy Revolution for the Treatment of Childhood Cancers.* Cancer Cell, 2017. **31**(4): p. 476-485.
26. Kumar, A., et al., *CXCL14 Promotes a Robust Brain Tumor-Associated Immune Response in Glioma.* Clin Cancer Res, 2022. **28**(13): p. 2898-2910.
27. Kmiecik, J., et al., *Elevated CD3+ and CD8+ tumor-infiltrating immune cells correlate with prolonged survival in glioblastoma patients despite integrated immunosuppressive mechanisms in the tumor microenvironment and at the systemic level.* J Neuroimmunol, 2013. **264**(1-2): p. 71-83.
28. Freeman, G.J., et al., *Engagement of the PD-1 immunoinhibitory receptor by a novel B7 family member leads to negative regulation of lymphocyte activation.* J Exp Med, 2000. **192**(7): p. 1027-34.
29. Sharma, P., et al., *The Next Decade of Immune Checkpoint Therapy.* Cancer Discov, 2021. **11**(4): p. 838-857.
30. Wei, S.C., C.R. Duffy, and J.P. Allison, *Fundamental Mechanisms of Immune Checkpoint Blockade Therapy.* Cancer Discov, 2018. **8**(9): p. 1069-1086.
31. Mathios, D., et al., *Anti-PD-1 antitumor immunity is enhanced by local and abrogated by systemic chemotherapy in GBM.* Sci Transl Med, 2016. **8**(370): p. 370ra180.
32. Reardon, D.A., et al., *Glioblastoma Eradication Following Immune Checkpoint Blockade in an Orthotopic, Immunocompetent Model.* Cancer Immunol Res, 2016. **4**(2): p. 124-35.
33. Atkins, M.B., et al., *Combination Dabrafenib and Trametinib Versus Combination Nivolumab and Ipilimumab for Patients With Advanced BRAF-Mutant Melanoma: The DREAMseq Trial-ECOG-ACRIN EA6134.* J Clin Oncol, 2023. **41**(2): p. 186-197.
34. Lim, M., et al., *Phase III trial of chemoradiotherapy with temozolomide plus nivolumab or placebo for newly diagnosed glioblastoma with methylated MGMT promoter.* Neuro Oncol, 2022. **24**(11): p. 1935-1949.
35. Dunkel, I.J., et al., *Nivolumab with or without ipilimumab in pediatric patients with high-grade CNS malignancies: Safety, efficacy, biomarker, and pharmacokinetics-CheckMate 908.* Neuro Oncol, 2023. **25**(8): p. 1530-1545.
36. Das, A., et al., *Combined Immunotherapy Improves Outcome for Replication-Repair-Deficient (RRD) High-Grade Glioma Failing Anti-PD-1 Monotherapy: A Report from the International RRD Consortium.* Cancer Discov, 2024. **14**(2): p. 258-273.

37. Pires da Silva, I., et al., *Efficacy and safety of anti-PD1 monotherapy or in combination with ipilimumab after BRAF/MEK inhibitors in patients with BRAF mutant metastatic melanoma.* J Immunother Cancer, 2022. **10**(7).
38. Atkins, M.B., *Update on the DREAMseq trial in melanoma.* Clin Adv Hematol Oncol, 2023. **21**(6): p. 304-306.
39. Xing, Y., Park, J.W., Grossauer, S., Wang, W., Panovska, D., Bui, B., Morales, D., Nirschl, J.J., Feng, ZP., Wei, R., Koeck, K., Nasajpour, E., Anderson, W., Harter, P.N., Filipski, K., Mulcahy Levy, J.M., Schreck, K., Walsh, K., Prolo, L.M., Walsh, K., Hambardzumyan, D., Petritsch, C.K. , *Clinically relevant concurrent BRAF and MEK inhibition alters differentiation states and sensitizes BRAF V600E-mutated high-grade gliomas to immune checkpoint blockade.* BioRxiv, 2023. **doi:10.1101/2023.02.03.526065**.
40. Cooper, Z.A., et al., *BRAF inhibition is associated with increased clonality in tumor-infiltrating lymphocytes.* Oncoimmunology, 2013. **2**(10): p. e26615.
41. Frederick, D.T., et al., *BRAF inhibition is associated with enhanced melanoma antigen expression and a more favorable tumor microenvironment in patients with metastatic melanoma.* Clin Cancer Res, 2013. **19**(5): p. 1225-31.
42. Wilmott, J.S., et al., *Selective BRAF inhibitors induce marked T-cell infiltration into human metastatic melanoma.* Clin Cancer Res, 2012. **18**(5): p. 1386-94.
43. Lee, J., et al., *Tumor stem cells derived from glioblastomas cultured in bFGF and EGF more closely mirror the phenotype and genotype of primary tumors than do serum-cultured cell lines.* Cancer Cell, 2006. **9**(5): p. 391-403.
44. Lerner, R.G., et al., *Targeting a Plk1-Controlled Polarity Checkpoint in Therapy-Resistant Glioblastoma-Propagating Cells.* Cancer Res, 2015. **75**(24): p. 5355-66.
45. Huillard, E., et al., *Cooperative interactions of BRAFV600E kinase and CDKN2A locus deficiency in pediatric malignant astrocytoma as a basis for rational therapy.* Proc Natl Acad Sci U S A, 2012. **109**(22): p. 8710-5.
46. Sugiarto, S., et al., *Asymmetry-defective oligodendrocyte progenitors are glioma precursors.* Cancer Cell, 2011. **20**(3): p. 328-40.
47. Reitman, Z.J., et al., *Mitogenic and progenitor gene programmes in single pilocytic astrocytoma cells.* Nat Commun, 2019. **10**(1): p. 3731.
48. Setoguchi, T. and T. Kondo, *Nuclear export of OLIG2 in neural stem cells is essential for ciliary neurotrophic factor-induced astrocyte differentiation.* J Cell Biol, 2004. **166**(7): p. 963-8.
49. Hemmati, H.D., et al., *Cancerous stem cells can arise from pediatric brain tumors.* Proc Natl Acad Sci U S A, 2003. **100**(25): p. 15178-83.
50. Castro, F., et al., *Interferon-Gamma at the Crossroads of Tumor Immune Surveillance or Evasion.* Front Immunol, 2018. **9**: p. 847.
51. Massa, C., et al., *Interferons and Resistance Mechanisms in Tumors and Pathogen-Driven Diseases-Focus on the Major Histocompatibility Complex (MHC) Antigen Processing Pathway.* Int J Mol Sci, 2023. **24**(7).
52. Zhang, Z., et al., *Interferon gamma-related gene signature based on anti-tumor immunity predicts glioma patient prognosis.* Front Genet, 2022. **13**: p. 1053263.
53. Li, H., et al., *Dysfunctional CD8 T Cells Form a Proliferative, Dynamically Regulated Compartment within Human Melanoma.* Cell, 2019. **176**(4): p. 775-789 e18.
54. Nduom, E.K., et al., *PD-L1 expression and prognostic impact in glioblastoma.* Neuro Oncol, 2016. **18**(2): p. 195-205.
55. Carbotti, G., et al., *IL-27 induces the expression of IDO and PD-L1 in human cancer cells.* Oncotarget, 2015. **6**(41): p. 43267-80.
56. Park, Y.J., et al., *IL-27 confers a protumorigenic activity of regulatory T cells via CD39.* Proc Natl Acad Sci U S A, 2019. **116**(8): p. 3106-3111.

57. Wertheimer, T., et al., *IL-23 stabilizes an effector T(reg) cell program in the tumor microenvironment.* Nat Immunol, 2024. **25**(3): p. 512-524.
58. Han, L., et al., *Interleukin 32 Promotes Foxp3(+) Treg Cell Development and CD8(+) T Cell Function in Human Esophageal Squamous Cell Carcinoma Microenvironment.* Front Cell Dev Biol, 2021. **9**: p. 704853.
59. Farhad, M., A.S. Rolig, and W.L. Redmond, *The role of Galectin-3 in modulating tumor growth and immunosuppression within the tumor microenvironment.* Oncoimmunology, 2018. **7**(6): p. e1434467.
60. Pasquini, L.A., et al., *Galectin-3 drives oligodendrocyte differentiation to control myelin integrity and function.* Cell Death Differ, 2011. **18**(11): p. 1746-56.
61. Thomas, L. and L.A. Pasquini, *Galectin-3-Mediated Glial Crosstalk Drives Oligodendrocyte Differentiation and (Re)myelination.* Front Cell Neurosci, 2018. **12**: p. 297.
62. Schreck, K.C., et al., *Deconvoluting Mechanisms of Acquired Resistance to RAF Inhibitors in BRAF(V600E)-Mutant Human Glioma.* Clin Cancer Res, 2021. **27**(22): p. 6197-6208.
63. Yao, T.W., et al., *Acquired resistance to BRAF inhibition in BRAFV600E mutant gliomas.* Oncotarget, 2017. **8**(1): p. 583-595.
64. Mulcahy Levy, J.M., et al., *Autophagy inhibition overcomes multiple mechanisms of resistance to BRAF inhibition in brain tumors.* Elife, 2017. **6**.
65. Michaud, K., et al., *Pharmacologic inhibition of cyclin-dependent kinases 4 and 6 arrests the growth of glioblastoma multiforme intracranial xenografts.* Cancer Res, 2010. **70**(8): p. 3228-38.
66. Dasgupta, T., et al., *Survival advantage combining a BRAF inhibitor and radiation in BRAF V600E-mutant glioma.* J Neurooncol, 2016. **126**(3): p. 385-93.
67. Olow, A., et al., *BRAF Status in Personalizing Treatment Approaches for Pediatric Gliomas.* Clin Cancer Res, 2016. **22**(21): p. 5312-5321.
68. Mulcahy Levy, J.M. and A. Thorburn, *Autophagy in cancer: moving from understanding mechanism to improving therapy responses in patients.* Cell Death Differ, 2020. **27**(3): p. 843-857.
69. Zahedi, S., et al., *Effect of early-stage autophagy inhibition in BRAF(V600E) autophagy-dependent brain tumor cells.* Cell Death Dis, 2019. **10**(9): p. 679.
70. Capper, D., et al., *DNA methylation-based classification of central nervous system tumours.* Nature, 2018. **555**(7697): p. 469-474.
71. Cabeza-Fernandez, S., et al., *Immune-stem cell crosstalk in the central nervous system: how oligodendrocyte progenitor cells interact with immune cells.* Immunol Cell Biol, 2023. **101**(1): p. 25-35.
72. Harrington, E.P., D.E. Bergles, and P.A. Calabresi, *Immune cell modulation of oligodendrocyte lineage cells.* Neurosci Lett, 2020. **715**: p. 134601.
73. Kirby, L., et al., *Oligodendrocyte precursor cells present antigen and are cytotoxic targets in inflammatory demyelination.* Nat Commun, 2019. **10**(1): p. 3887.
74. Falcao, A.M., et al., *Disease-specific oligodendrocyte lineage cells arise in multiple sclerosis.* Nat Med, 2018. **24**(12): p. 1837-1844.
75. Linnerbauer, M., et al., *PD-L1 positive astrocytes attenuate inflammatory functions of PD-1 positive microglia in models of autoimmune neuroinflammation.* Nat Commun, 2023. **14**(1): p. 5555.
76. Constantinescu, C.S., et al., *Astrocytes as antigen-presenting cells: expression of IL-12/IL-23.* J Neurochem, 2005. **95**(2): p. 331-40.
77. Younes-Rapozo, V., et al., *A role for the MAPK/ERK pathway in oligodendroglial differentiation in vitro: stage specific effects on cell branching.* Int J Dev Neurosci, 2009. **27**(8): p. 757-68.

78. Ishii, A., et al., *Role of ERK1/2 MAPK signaling in the maintenance of myelin and axonal integrity in the adult CNS.* J Neurosci, 2014. **34**(48): p. 16031-45.
79. Michel, K., et al., *Translational control of myelin basic protein expression by ERK2 MAP kinase regulates timely remyelination in the adult brain.* J Neurosci, 2015. **35**(20): p. 7850-65.
80. Marques, S., et al., *Oligodendrocyte heterogeneity in the mouse juvenile and adult central nervous system.* Science, 2016. **352**(6291): p. 1326-1329.
81. Wang, J., et al., *CD133/CD140a-based isolation of distinct human multipotent neural progenitor cells and oligodendrocyte progenitor cells.* Stem Cells Dev, 2013. **22**(15): p. 2121-31.
82. Wang, V.E., et al., *Adaptive Resistance to Dual BRAF/MEK Inhibition in BRAF-Driven Tumors through Autocrine FGFR Pathway Activation.* Clin Cancer Res, 2019. **25**(23): p. 7202-7217.
83. Liu, L., et al., *The BRAF and MEK Inhibitors Dabrafenib and Trametinib: Effects on Immune Function and in Combination with Immunomodulatory Antibodies Targeting PD-1, PD-L1, and CTLA-4.* Clin Cancer Res, 2015. **21**(7): p. 1639-51.
84. Gonin, J., et al., *Expression of IL-27 by tumor cells in invasive cutaneous and metastatic melanomas [corrected].* PLoS One, 2013. **8**(10): p. e75694.
85. Diakowska, D., et al., *Concentration of serum interleukin-27 increase in patients with lymph node metastatic gastroesophageal cancer.* Adv Clin Exp Med, 2013. **22**(5): p. 683-91.
86. Chandramohan, V., et al., *Improved efficacy against malignant brain tumors with EGFRwt/EGFRvIII targeting immunotoxin and checkpoint inhibitor combinations.* J Immunother Cancer, 2019. **7**(1): p. 142.
87. Lan, H. and Y. Sun, *Tumor Suppressor FBXW7 and Its Regulation of DNA Damage Response and Repair.* Front Cell Dev Biol, 2021. **9**: p. 751574.
88. Nabeki, B., et al., *Interleukin-32 expression and Treg infiltration in esophageal squamous cell carcinoma.* Anticancer Res, 2015. **35**(5): p. 2941-7.
89. Jackson, C.M., J. Choi, and M. Lim, *Mechanisms of immunotherapy resistance: lessons from glioblastoma.* Nat Immunol, 2019. **20**(9): p. 1100-1109.
90. Blomberg, E., et al., *Programmed death ligand 1 gene silencing in murine glioma models reveals cell line-specific modulation of tumor growth in vivo.* Neurooncol Adv, 2022. **4**(1): p. vdac148.
91. *Tovorafenib (Ojemda) for pediatric low-grade glioma.* Med Lett Drugs Ther, 2024. **66**(1704): p. e97-e98.
92. Simonds, E.F., et al., *Deep immune profiling reveals targetable mechanisms of immune evasion in immune checkpoint inhibitor-refractory glioblastoma.* J Immunother Cancer, 2021. **9**(6).
93. Arrieta, V.A., et al., *ERK1/2 phosphorylation predicts survival following anti-PD-1 immunotherapy in recurrent glioblastoma.* Nat Cancer, 2021. **2**(12): p. 1372-1386.
94. Long, G.V., et al., *Antitumor activity of ipilimumab or BRAF +/- MEK inhibition after pembrolizumab treatment in patients with advanced melanoma: analysis from KEYNOTE-006.* Ann Oncol, 2022. **33**(2): p. 204-215.
95. Huynh, S., et al., *Combined Therapy with Anti-PD1 and BRAF and/or MEK Inhibitor for Advanced Melanoma: A Multicenter Cohort Study.* Cancers (Basel), 2020. **12**(6).

Acknowledgments:

We would like to thank Sista Sugiarto, Anne Marie Barrette, and Caitlynn Tran for their excellent technical assistance. We thank Egbert Lu and Erin Simmons and the UCSF Flow Cytometry Core for help with mass cytometry and the UCSF Brain Tumor Tissue Core and Stanford Neuroscience Tissue Bank for providing patient samples. We also thank Mr. Steve Avolicino from Histo-Tec Laboratory Inc. for tissue processing and immunohistochemical staining. We acknowledge the use of Stanford facilities including Stanford Veterinary Service Center, Neurosciences Preclinical Imaging Lab (Dr. Jieun Kim), Neuroscience Microscopy Service (Dr. Gordon Wang), Human Pathology/Histology Service Center (Pauline Chu), Stanford Human Immune Monitoring Centre (Molly Miranda), and Anita Metha-Damani and Xue Gong (Synthekine) for advice on T cell profiles.

Funding

This work was supported by the

National Institute of Health R21 NS099836 (C.K.P)

National Institute of Health R01 NS080619 (C.K.P)

National Institute of Health R01 CA164746 (C.K.P.)

National Institute of Health 17X074 (C.K.P.)

Neurosciences Preclinical Imaging Lab Pilot Grant 2022 (C.K.P.)

Stanford Women's Health and Sex Differences Center (WHSDM) Seed Grant (C.K.P)

BRAF LGG consortium research fund (C.K.P; K.M.W.)

Stanford Cancer Institute (C.K.P)

National Institute of Health U54 CA 261717

Shurl and Kay Curci Foundation (L.M.P.)

Stanford Maternal & Child Health Research Institute (L.M.P.)

Chambers-Okamura Faculty Scholar in Pediatric Neurosurgery (L.M.P).

National Institutes of Health P30AG066515 (J.J.N)

Author Contributions:

Conceptualization: CKP, SG

Data curation: YLX, JWP, DP, BB, DM, ZPF, RW, KMW, JX

Formal Analysis: YLX, SG, JWP, DP, BB, DM, ZPF, KK

Funding acquisition: CKP, LMP

Investigation: YLX, DP, BB, DM, JJN

Methodology: YLX, DP, DM, ZPF, KMW

Project administration: CKP

Resources: CKP, DH, WT, JMML, KF, LMP, KM, GAG, ML

Software: CKP, YLX

Supervision: CKP, DH

Validation: BB, DM, RW, KK, PH, KF, KMW

Visualization: JJN, KMW

Writing-original draft: CKP, YLX, DP, JWP

Writing-review & editing: CKP, YLX, KMW

Competing Interests:

Authors declare that they have no competing interests.